

Functional Imaging Constrained Diffusion for Brain PET Synthesis from Structural MRI

Minhui Yu, Mengqi Wu, Ling Yue, Andrea Bozoki, Mingxia Liu, *Senior Member, IEEE*

Abstract—Magnetic resonance imaging (MRI) and positron emission tomography (PET) are increasingly used in multimodal analysis of neurodegenerative disorders. While MRI is broadly utilized in clinical settings, PET is less accessible. Many studies have attempted to use deep generative models to synthesize PET from MRI scans. However, they often suffer from unstable training and inadequately preserve brain functional information conveyed by PET. To this end, we propose a functional imaging constrained diffusion (FICD) framework for 3D brain PET image synthesis with paired structural MRI as input condition, through a new constrained diffusion model (CDM). The FICD introduces noise to PET and then progressively removes it with CDM, ensuring high output fidelity throughout a stable training phase. The CDM learns to predict denoised PET with a functional imaging constraint introduced to ensure voxel-wise alignment between each denoised PET and its ground truth. Quantitative and qualitative analyses conducted on 293 subjects with paired T1-weighted MRI and ^{18}F -fluorodeoxyglucose (FDG)-PET scans suggest that FICD achieves superior performance in generating FDG-PET data compared to state-of-the-art methods. We further validate the effectiveness of the proposed FICD on data from a total of 1,262 subjects through three downstream tasks, with experimental results suggesting its utility and generalizability.

Index Terms—Brain, Image Synthesis, PET, Structural MRI, Diffusion Model.

1 INTRODUCTION

BRAIN magnetic resonance imaging (MRI) and positron emission tomography (PET) offer a synergistic diagnosis of the brain. MRI, with its detailed structural imaging capabilities, is one of the main processes in clinical diagnostics of neurodegenerative disorders [1–3]. PET provides unique insights into the brain’s metabolic patterns and neuronal activity through specific radioactive tracers [4–6]. Conducting a multimodal study with these two imaging techniques proves to be especially advantageous in the exploration of neurodegenerative disorders, due to the intricate interplay between brain anatomy and its biochemical processes [7, 8]. Despite their combined value, the acquisition of brain PET lags behind MRI, primarily due to PET’s higher operational costs and complexities in handling radioactive materials [9]. The frequent unavailability of brain PET scans poses challenges to the progress of multimodal studies [10, 11].

To address this modality-missing issue, numerous efforts have explored employing deep generative models to synthesize PET images from MRI scans. Generative adversarial networks (GANs) have been widely used due to their capability of high-fidelity image generation [11–14]. These approaches frequently encounter issues with training instability attributed to their training nature and also suffer from limited diversity in the generated outputs due to mode

collapse [15]. Variational autoencoder (VAE) models, including hybrids like VAEGAN, are also popular in medical image synthesis due to their ability to handle complex data structures effectively [16, 17]. However, VAE models usually suffer from image blurriness and face posterior collapse, where a subset of the latent space becomes redundant and does not contribute to the data generation process [18].

Diffusion models have gained significant attention as a robust type of deep generative model. By initially introducing noise to data and then progressively denoising it through iterative processes [19, 20], diffusion models have been applied in a wide range of fields and produce better outcomes than other types of generative models [21, 22]. Most recently, it has gained increasing interest in medical research for cross-modality image translation [23]. However, the optimization of diffusion models only relies on the constraint of noise, yielding an indirect estimation of image outputs, which is inadequate to generate unique outcomes. This outcome uniqueness is particularly critical in 3D PET synthesis, since voxel intensities of PET images convey essential brain functional information (e.g., measurement of regional glucose consumption in ^{18}F -fluorodeoxyglucose (FDG)-PET and detection of amyloid plaques in amyloid PET) that is crucial for brain disorder analysis [24]. Intuitively, it is meaningful to introduce an image-level constraint to ensure the precise one-to-one voxel correspondence between each synthetic PET image and its ground truth, helping improve the output uniqueness of diffusion models.

To this end, we propose a functional imaging constrained diffusion (FICD) framework for 3D PET image synthesis from structural MRI, through a new constrained diffusion model (CDM). The FICD framework is designed to generate samples with the Markov chain transition of a denoising diffusion model, to synthesize PET images with the MRI as a condition. As illustrated in Fig. 1 (a), it consists of a

- M. Yu, M. Wu and M. Liu are with the Department of Radiology and Biomedical Research Imaging Center (BRIC), University of North Carolina at Chapel Hill, Chapel Hill, NC 27599, USA. M. Yu and M. Wu are also with the Joint Department of Biomedical Engineering, University of North Carolina at Chapel Hill and North Carolina State University, Chapel Hill, NC 27599, USA. L. Yue is with the Department of Geriatric Psychiatry, Shanghai Mental Health Center, Shanghai Jiao Tong University School of Medicine, Shanghai 200240, China. A. Bozoki is with the Department of Neurology, University of North Carolina at Chapel Hill, Chapel Hill, NC 27599, USA.
- Corresponding author: M. Liu (Email: mxliu@med.unc.edu).

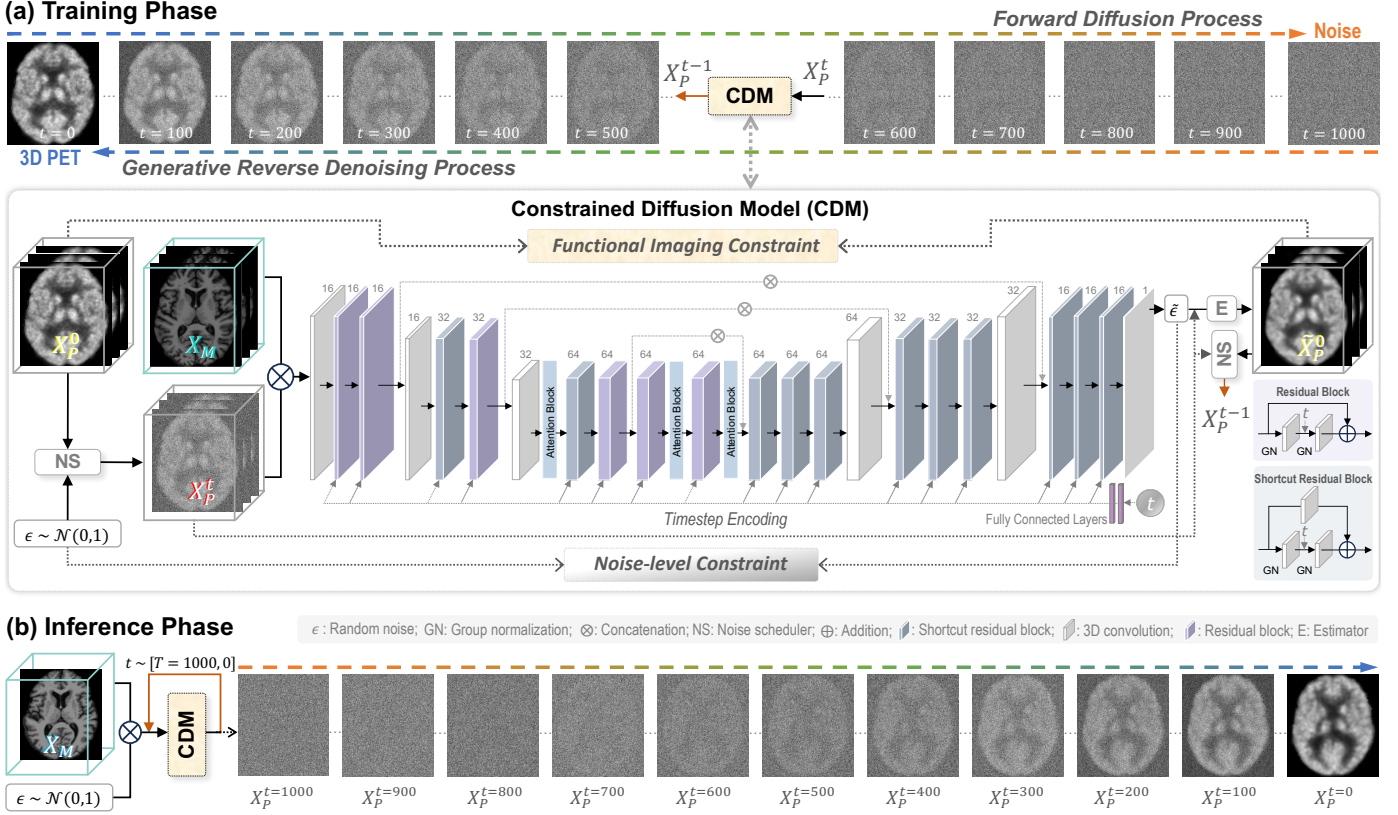


Fig. 1. Illustration of the proposed functional imaging constrained diffusion (FICD) framework for 3D brain PET image synthesis with paired structural MRI as the condition. (a) The training phase consists of a *forward diffusion process* that incrementally adds noise to an input PET image, and a *generative reverse denoising process* that gradually removes the noise. The MRI condition and noise-corrupted PET are input to the proposed constrained diffusion model (CDM) to predict the noise on PET, then the noise is further used to estimate the denoised PET in the previous timestep and in the final timestep. The outputs of CDM are optimized by a unique functional imaging constraint and a noise-level constraint, respectively. (b) In the inference phase, an MRI and a pure noise are input to the CDM, which progressively removes the noise to generate a synthetic PET image.

forward diffusion process that incrementally adds noise to an input PET image, and a *generative reverse denoising process* that gradually removes the noise with CDM. Specifically, the condition (*i.e.*, MRI) and noise-corrupted PET are input to the CDM to predict the noise on PET, then the noise is further used to estimate the denoised PET in the previous timestep and in the final timestep. The outputs of CDM are optimized by a new functional imaging constraint and a noise-level constraint, respectively. The functional imaging constraint is designed to ensure *voxel-wise alignment* between a synthesized PET image and its ground truth. Extensive experiments are performed on T1-weighted MRI and PET scans in both image synthesis and three downstream tasks (*i.e.*, forecasting the progression of brain diseases, predicting future cognitive functions, and generating amyloid PET images), with experimental results indicating the superiority of our method over several state-of-the-arts.

The major contributions of this work can be summarized in the following.

- A new generative framework called functional imaging constrained diffusion (FICD) is developed to synthesize 3D PET from structural MRI, helping alleviate the modality-missing issue in multimodal studies. Quantitative and qualitative results show that FICD is capable of producing high-quality PET images.
- A functional imaging constraint is designed to encourage voxel-wise alignment between an estimated

PET and its ground truth, further constraining the denoising process. This is different from traditional diffusion models that only rely on noise constraints for optimization. Experimental results suggest that this constraint improves the fidelity of synthesized images and significantly reduces output variability.

- Extensive experiments are conducted to evaluate the utility of synthesized PET images in two downstream tasks: forecasting the progression of preclinical Alzheimer’s disease (AD) and predicting cognitive function at future time points. The experimental results demonstrate the improvements achieved by our method in multimodal analysis of preclinical AD.
- We further adapt the FICD model, initially trained on FDG-PET, to accommodate PET with three common amyloid radiotracers (*i.e.*, Pittsburgh Compound-B, ^{18}F -flutemetamol, and Florbetapir), by fine-tuning this model to generate PET scans with these tracers. This adaptation highlights the model’s flexibility and generalizability across various problem settings.

The remainder of this paper is organized as follows. We review the most relevant studies in Section 2. In Section 3, we introduce the details of the proposed method. In Section 4, we present data involved in this work, competing methods, experimental settings, and experimental results. We further study the influence of several key components on the performance of the proposed method in Section 5.

This paper is finally concluded in Section 6.

2 RELATED WORK

2.1 Multimodal Medical Image Analysis

Neuroimaging biomarkers provided by MRI and PET are among the most pivotal tools for monitoring Alzheimer’s disease (AD) progression and understanding its underlying pathology [25]. While structural MRI helps unveil brain atrophy, ^{18}F -fluorodeoxyglucose (FDG)-PET can capture regional hypometabolism, and amyloid PET helps detect amyloid plaque accumulation in the brain [26]. Since each modality offers unique insights into brain structure and function, the integration of these modalities significantly improves disease progression prediction [10, 27, 28]. Walhovd et al. [27] report that MRI and FDG-PET complement each other due to their varied sensitivity to memory performance across healthy aging and various stages of cognitive decline. Jack et al. [28] observe that using amyloid PET and MRI together can enhance clinical diagnosis compared to using a single modality. Sharma et al. [10] highlight that missing data or incomplete modality are common challenges in multimodal analyses, impacting the comprehensive integration and interpretation of multimodal imaging data. In particular, while MRI is widely used in clinical settings, PET scans are less readily available due to their high cost and requirement for radioactive tracers [9, 24].

Some previous studies attempt to solve the modality-missing issue by imputing those missing neuroimage features. Abdelaziz et al. [29] employ linear interpolation to address missing modalities. Ritter et al. [30] utilize a hybrid approach combining mean imputation and the Expectation-Maximization (EM) algorithm to impute features for missing modalities. Some studies [31, 32] employ multi-view learning methods to make use of samples with incomplete modalities, without directly imputing those missing feature values. However, these methods generally focus on predefined features that are specifically engineered by experts to represent neuroimages. Considering these human-engineered features may not be sufficient to represent the rich information in brain functional and structural images, direct synthesis of missing neuroimages could provide a more effective solution to this problem [12–14, 33].

2.2 Cross-Modality Medical Image Translation

Recent efforts have explored employing deep generative models for medical image synthesis to impute those missing modalities, with generative adversarial networks (GANs) becoming one of the most popular methods [34]. The architecture of a typical GAN model comprises two components: a generator and a discriminator. The generator aims to mimic the distribution of real data, whereas the discriminator functions as a binary classifier to discern between synthetic and real samples through continuous optimization. These two components are engaged in a competitive yet mutually beneficial interaction. Many studies have utilized GANs to synthesize PET images from structural MRI scans. Hu et al. [12] introduce a bidirectional mapping GAN that incorporates semantic information derived from PET images into the latent space learned by GAN, to facilitate

the utilization of both image contexts and latent vectors. Zhang et al. [13] develop a brain PET GAN, a 3D end-to-end framework that employs a multiple convolution U-Net [35] generator architecture, augmented with gradient profile loss and structural similarity index measure loss. Vega et al. [14] employ a conditional GAN architecture that inputs a pair of MRI and synthetic PET images into the discriminator to determine if it is synthetic or real. A critical challenge in training GAN models is their inherent instability, where the generator and discriminator engage in a complex dynamic that can be difficult to balance effectively. This often manifests in issues such as mode collapse, where the generator produces a limited variety of samples [15].

Variational autoencoder (VAE) is another type of generative model. They employ deep neural networks to first encode input data into a latent space with predefined distributions, optimized by maximizing the evidence lower bound between the encoded distributions and a prior, and then decode from this space to reconstruct the input [36]. The integration of VAE with GANs, known as VAEGANs, can further enhance its performance and has gained widespread utilization [37]. Yang et al. [17] leverage VAEGAN to create cross-domain and multi-contrast MR images from CT scans. Similarly, Li et al. [16] utilize VAEGAN to generate arterial spin labeling (ASL) images from structural MRI and demonstrate an enhancement in diagnosis accuracy facilitated by synthesized ASL images. While achieving notable success, VAEs also present distinct limitations, since they are prone to producing outputs lack of image sharpness [38]. Additionally, these models tend to suffer from posterior collapse, where a subset of the latent space becomes redundant and does not contribute to the data generation process [39].

Diffusion models have recently gained increasing attention in image synthesis [19, 20, 40]. They are distinguished by their high training stability and capability to generate images of exceptional quality, offering solutions to the challenges commonly faced by GANs and VAEs [21, 22]. A few studies have attempted to use them to synthesize missing medical images [33, 41]. Lyu et al. [41] utilize the Denoising Diffusion Probabilistic Model (DDPM) and score-based diffusion model to translate MR images into computed tomography (CT) scans, tackling output uncertainty through Monte-Carlo sampling [41]. Their findings demonstrate that diffusion models outperform traditional convolutional neural networks and GANs in this modality conversion task. Xie et al. [33] employ a joint diffusion attention model to generate synthetic PET images from high-field and ultra-high-field MRI scans, utilizing MRIs as a condition. However, diffusion models tend to produce diverse outputs due to the randomness of input noise [41]. This output variability may not be advantageous for cross-modality medical image translation where consistency and accuracy are crucial. In particular, the outcome uniqueness is critical in brain PET synthesis since image voxel intensities convey functional measures of brain activity, such as regional glucose consumption in FDG-PET and amyloid plaques in amyloid PET images [24]. In this work, we introduce a functional imaging constraint to guide the diffusion model toward generating more consistent outputs, enhancing its suitability for medical image synthesis.

3 METHODOLOGY

3.1 Problem Formulation

This work focuses on synthesizing 3D brain PET images based on structural MRI scans. We denote X_M as a 3D MR image and X_P as its corresponding 3D PET image. We aim to train a model that can map a structural MRI to its real PET image, denoted as $f: \{\mathbf{x} \in X_M\} \rightarrow \{\mathbf{x}' \in X_P\}$. In the inference phase, an MRI scan can be input to the trained model to generate a PET image, thus helping alleviate the modality-missing issue. Considering the diffusion model's high training stability and the capability to generate high-quality images through learning Markov chain transitions for sample generation, we propose to use the diffusion model to synthesize 3D PET images with the guidance of structural MRI condition, as depicted in Fig. 1. The specifics of the proposed method are introduced as follows.

3.2 Proposed Methodology

3.2.1 Overview

As shown at the top of Fig. 1 (a), our functional imaging constrained diffusion (FICD) framework consists of a *forward diffusion process* that incrementally adds Gaussian noise to the PET image, and a *generative reverse denoising process* that progressively removes the noise. Given T timesteps, the forward diffusion process is a Markov chain, defined as:

$$q(X_P^1, \dots, X_P^T | X_P^0) := \prod_{t=1}^T q(X_P^t | X_P^{t-1}), \quad (1)$$

where q is the posterior distribution, X_P^0 is the real PET image and $\{X_P^1, \dots, X_P^T\}$ is the disturbed samples from timestep 1 to T . The distribution of disturbed samples at timestep t can be formulated with Gaussian transitions:

$$q(X_P^t | X_P^0) = \mathcal{N}\left(X_P^t; \sqrt{\bar{\alpha}^t} \cdot X_P^0, (1 - \bar{\alpha}^t) \cdot \mathbf{I}\right), \quad (2)$$

where $\mathcal{N}(\mu, \sigma)$ is Gaussian distribution with mean μ and variance σ , while $\bar{\alpha}^t := \prod_{s=1}^t \alpha^s$ is a time-dependent hyperparameter and \mathbf{I} is the identity matrix indicating isotropic variance. In the generative reverse denoising process, the proposed constrained diffusion model (CDM) predicts noise on each sample on timestep t and removes it to predict X_P^{t-1} from X_P^t iteratively, where $t \sim [T, 0]$ and X_P^t is the synthesized PET at timestep t .

The bottom part of Fig. 1 (a) shows the architecture of CDM, which contains three steps. 1) Input processing: At timestep t , a noise scheduler NS introduces random noise $\epsilon \sim N(0, 1)$ into the PET image X_P^0 to create the input noisy image X_P^t , following the distribution in Eq. (2). This image is then concatenated with a condition image X_M , and the model is also fed with the timepoint t to determine the state of the noise scheduler. 2) Neural network learning: The input is first downsampled, and then upsampled to produce the output noise $\tilde{\epsilon}$, with the downsampled features integrated into the upsampling, and enhanced with attention blocks. 3) Output processing: With the predicted noise $\tilde{\epsilon}$, denoised X_P^{t-1} and \tilde{X}_P^0 is estimated through an estimator \mathbf{E} and a new NS. Additionally, Fig. 1 (b) depicts the inference phase where the trained model generates a synthetic PET image starting from pure noise (with an MRI as a condition).

Condition. To guide the synthesizing process toward a specific output, a condition can be introduced alongside the

input noisy image. In cross-modality image translation, the source modality can serve as a condition to facilitate the synthesis of the target modality. In FICD, we achieve this by concatenating the paired MRI X_M with the noisy PET image, both having the same image dimension, as the input.

An alternative approach could be using the gradient image of MRI as the condition. As proposed in [42], when the diffusion denoising model is used to predict gradient, it can yield a higher training efficiency. Given that PET images typically lack distinct gradient information due to their functional imaging nature, one can alternatively use the gradient of MRI ∇X_M that conveys rich anatomical information about the brain as the condition. A comparative analysis of this gradient-based approach with the direct use of MR images as the condition will be detailed in Section 5.4.

Training Phase. In the *training phase*, instead of iterating through every timestep, an intermediate timestep t is randomly selected for each input subject to learn the denoising from t to $t-1$. To achieve this, a random Gaussian noise $\epsilon \sim N(0, 1)$ is employed to corrupt the data point X_P^0 , i.e., the PET scan, with the noise scheduler NS. By reparameterizing α^t in Eq. (2) [20], this corruption process can be mathematically expressed as:

$$X_P^t = \sqrt{\alpha^t} X_P^0 + \epsilon \sqrt{1 - \alpha^t}. \quad (3)$$

The corrupted data X_P^t is then concatenated with the corresponding condition, i.e., the MRI scan, to form the input for the neural network. With the timestep t embedded, the neural network outputs the predicted noise $\tilde{\epsilon}$ at t . A noise-level constraint using mean squared error loss is incorporated to encourage the estimated noise to be close to the real noise ϵ :

$$L_N = \frac{1}{n} \sum_{i=1}^n (\epsilon - \tilde{\epsilon}((X_M)^i, (X_P^t)^i, t))^2, \quad (4)$$

where n is the training sample size, while $(X_M)^i$ and $(X_P^t)^i$ denote the MRI and noisy PET data for the i -th subject.

3.2.2 Functional Imaging Constraint

In a vanilla denoising diffusion model [20], while the noisy input is composed of the original image and input noise ϵ , only the predicted noise $\tilde{\epsilon}$ is constrained in optimization. Therefore, the model only receives indirect information about the images it is tasked to synthesize, which may not be sufficient to ensure the production of images with voxel-level correspondence to the ground truth. Moreover, relying solely on noise for constraints introduces uncertainty throughout the entire framework, potentially affecting its performance. To improve synthesis and reduce uncertainty, we propose to use a *functional imaging constraint* to guide the model training, ensuring the similarity between the synthetic PET and the real PET image at each timestep.

Specifically, we propose to generate a synthetic PET at the timestep t through an image estimator \mathbf{E} , which can be achieved by reformulating Eq. (3) as follows:

$$\tilde{X}_P^0 = \frac{X_P^t - \sqrt{1 - \bar{\alpha}^t} \tilde{\epsilon}(X_M, X_P^t, t)}{\sqrt{\bar{\alpha}^t}}. \quad (5)$$

With the estimated PET image \tilde{X}_P^0 , we employ an l_1 loss in this functional imaging constraint, defined as:

$$L_I = \frac{1}{n} \sum_{i=1}^n |X_P^0 - \tilde{X}_P^0|, \quad (6)$$

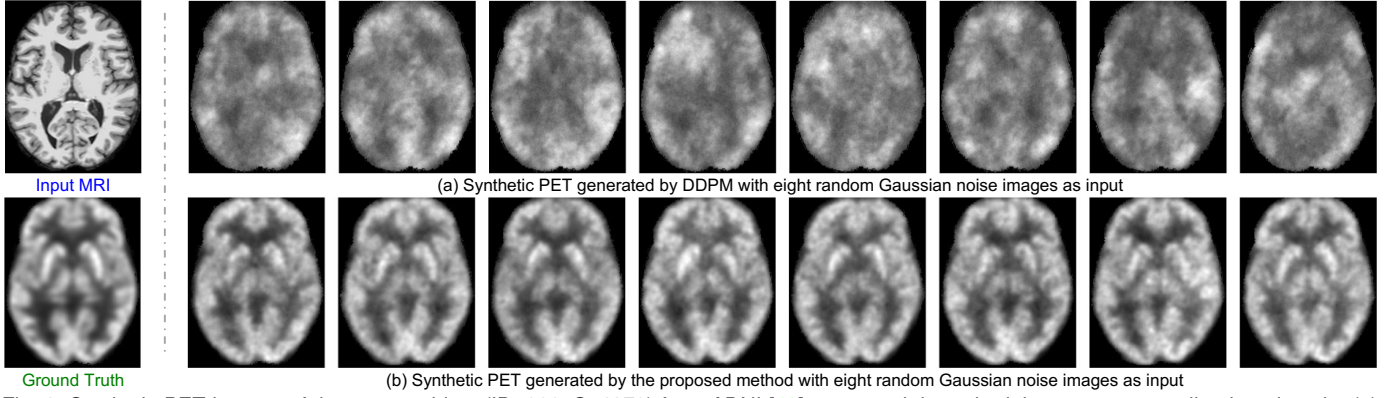


Fig. 2. Synthetic PET images of the same subject (ID: 002_S_4270) from ADNI [43] generated through eight separate sampling iterations by (a) DDPM [20] and (b) our FICD, with each iteration introducing new random noise. The input MRI and the ground-truth PET are displayed on the left.

which aims to minimize the voxel-wise discrepancy between the estimated image \tilde{X}_P^0 and the real PET X_P^0 . This encourages the PET generated in the intermediate process of the diffusion model to be close to the real one, thus helping preserve the functional information conveyed in PET.

3.2.3 Constrained Diffusion Model

By incorporating the above-mentioned functional imaging constraint, we develop a constrained diffusion model (CDM), used in each timestep of our FICD. At timestep t , the input of CDM contains the perturbed PET image X_P^t and the paired 3D MRI X_M that is integrated as a conditional variable. During training, the output of CDM is fed into an image estimator \mathbf{E} to generate a PET \tilde{X}_P^0 (with noise removed) to facilitate the computation of functional imaging constraint. During inference (see Section 3.3), the \tilde{X}_P^0 is fed into a noise scheduler with X_P^t to generate a denoised PET X_P^{t-1} (with noise removed according to the timestep). With Eq. (4) and Eq. (6), the CDM will be optimized by minimizing the following hybrid loss:

$$L = L_N + L_I. \quad (7)$$

The bottom part of Fig. 1 (a) illustrates the network architecture of the CDM, consisting of three downsampling blocks and three upsampling blocks. Each of the three downsampling blocks contains a convolutional layer to reduce spatial dimensions and two residual sub-blocks that use skip connections. Each residual sub-block includes two convolutional layers with each of them going through a group normalization, a timestep embedding, and a shortcut connection [20]. The timestep embedding component projects the encoded timestep features to align with the number of feature channels, thereby integrating the timestep information into feature learning. The number of feature channels increases throughout the downsampling blocks, from 16 to 32, then to 64. To accommodate the increment in feature channel numbers, the architecture includes two variations of residual blocks. When the number of input feature channels matches the output, the input and output are summed for a skipping connection. If the output feature channels exceed the number of input channels, a convolutional layer is introduced to the shortcut connection to align the dimensions accordingly. The three upsampling blocks work in reverse to downsampling, enlarging image dimensions while decreasing the number of feature channels.

The output from each downsampling block is concatenated with the corresponding upsampling block to preserve image details [35]. This architecture is enhanced by incorporating attention blocks that perform self-attention on the learned intermediate features, thereby emphasizing the important features for improved model performance. Each attention block has 8 attention heads with 64 channels [44].

3.3 Inference Phase

As shown in Fig. 1 (b), to obtain synthesized PET from MRI, CDM is applied to remove noise from the input through generative reverse denoising process, starting with Gaussian noise $\epsilon \sim \mathcal{N}(0, 1)$ concatenated with MRI of matching dimensions as the input. With the input noisy image X_P^t (pure noise ϵ when $t = T$) and the noise scheduler NS at timestep t , and the estimated output \tilde{X}_P^0 in Eq. (5), the noise distribution [20] at timestep $t - 1$ can be written as:

$$q(X_P^{t-1} | X_P^t, \tilde{X}_P^0) = \mathcal{N}(X_P^{t-1}; \tilde{\mu}^t(X_P^t, \tilde{X}_P^0), \tilde{\alpha}^t \mathbf{I}), \quad (8)$$

where

$$\tilde{\mu}^t(X_P^t, \tilde{X}_P^0) := \frac{\sqrt{\tilde{\alpha}^{t-1}}(1 - \alpha^t)}{1 - \tilde{\alpha}^t} \tilde{X}_P^0 + \frac{\sqrt{\alpha^t}(1 - \tilde{\alpha}^{t-1})}{1 - \tilde{\alpha}^t} X_P^t, \quad (9)$$

$$\tilde{\alpha}^t = \frac{1 - \tilde{\alpha}^{t-1}}{1 - \tilde{\alpha}^t} (1 - \alpha^t). \quad (10)$$

The sample result of X_P^{t-1} , serving as the noisy PET input for the subsequent iteration, can therefore be formulated as:

$$X_P^{t-1} = \frac{1}{\sqrt{\alpha^t}} \left(X_P^t - \frac{1 - \alpha^t}{\sqrt{1 - \tilde{\alpha}^t}} \tilde{\epsilon}(X_M, X_P^t, t) \right) + \sigma^t z, \quad (11)$$

where $z \sim \mathcal{N}(0, 1)$ and σ^t denotes the variance [20]. Through $T = 1,000$ inference timesteps, the model gradually removes noise and ultimately yields the PET image.

During inference, the randomness of noise would introduce uncertainty to the output. This is a common challenge in denoising diffusion models for medical image synthesis [41]. Figure 2 shows eight outputs for the same subject, each image synthesized by DDPM [20] and the proposed FICD using different instances of Gaussian random noise. From Fig. 2 (a), one can observe that each of the synthesized images generated by DDPM is different. Figure 2 (b) suggests that the synthesized images generated by FICD have an overall resemblance, which could be attributed

TABLE 1

Clinical information of subjects used in this work. Mini-mental state examination (MMSE) and clinical dementia rating (CDR) scores are presented as mean \pm standard deviation. Four types of radiotracers are involved in PET imaging: ^{18}F -fluorodeoxyglucose (FDG), Pittsburgh Compound-B (PiB), ^{18}F -flutemetamol (FLUTE), and Flortbetapir (AV45).

Task	Cohort	Group	Class	Subject #	Radiotracer	MMSE	CDR
1	ADNI	Training	CN	263	FDG	–	–
		Test	CN	30	FDG	–	–
2&3	ADNI	Training	AD	359	FDG	23.31 ± 2.05	4.29 ± 1.81
		Training	CN	436	FDG	29.08 ± 1.12	0.04 ± 0.19
	CLAS-SCD	Test	pSCD	24	FDG	26.75 ± 2.55	–
		Test	sSCD	51	FDG	27.73 ± 2.15	–
	ADNI-SMC	Test	pSMC	19	FDG	28.95 ± 1.36	1.45 ± 1.14
		Test	sSMC	42	FDG	29.07 ± 0.99	0.67 ± 0.24
4	AIBL	Fine-tuning	CN	107	PiB	–	–
		Test	CN	12	PiB	–	–
	AIBL	Fine-tuning	CN	128	FLUTE	–	–
		Test	CN	15	FLUTE	–	–
	AIBL	Fine-tuning	CN	62	AV45	–	–
		Test	CN	7	AV45	–	–

to the proposed functional imaging constraint to reduce output uncertainty to some extent. In addition, a common post-processing strategy to address this issue is to employ the Monte-Carlo (MC) sampling method [41], by repeating the denoising process multiple times to generate multiple synthetic outputs and using the averaged results as the final output. This helps to further mitigate the effects of randomness in image synthesis. We will discuss the influence of the MC sampling strategy in Section 5.2.

3.4 Implementation Details

The implementation of FICD utilizes the PyTorch-based MONAI framework [45] within a Python 3.11.5 environment and an RTX 3090 GPU (24 GB memory). The training of FICD involves 50 epochs, and batch size is set as 2. Adam optimizer is employed with a learning rate established at 5×10^{-5} . In line with [20], we empirically set the timestep T as 1,000 and linearly increase scheduler $1 - \alpha^t$ from 0.0005 to 0.0195. All 3D MRI and PET scans used for training image synthesis models in this work are paired for each subject.

4 EXPERIMENT

4.1 Subjects and Multimodal Image Preprocessing

Three cohorts are used for performance evaluation: 1) the Alzheimer’s Disease Neuroimaging Initiative (ADNI) [43], 2) the Chinese Longitudinal Aging Study (CLAS) [46], and 3) the Australian Imaging, Biomarkers and Lifestyle (AIBL) study [47]. This work uses baseline imaging data from the three cohorts.

1) **ADNI**. A total of 856 subjects from ADNI are utilized in this study, including 359 individuals diagnosed with Alzheimer’s disease (AD), 436 cognitively normal (CN) individuals, and 61 subjects identified as clinically normal but exhibiting significant memory concerns (SMC), which may indicate preclinical AD [48]. Among the SMC subjects, based on 5-year follow-up results, 19 are identified as having progressive significant memory concern (pSMC), and 42 subjects are classified as stable significant memory concern (sSMC). Specifically, as all of these subjects exhibit

SMC at baseline time, those who maintain SMC over a 5-year follow-up are categorized as sSMC, while those who progress to mild cognitive impairment (MCI) or AD during the same period are classified as pSMC. Among all of those subjects, 293 CN subjects, 240 AD subjects, and all SMC subjects have both baseline T1-weighted structural MRI and ^{18}F -fluorodeoxyglucose (FDG)-PET scans available. The remaining subjects only have MRI data.

2) **CLAS**. The CLAS is a de-identified database, designed to provide information about the cognitive, mental, and psychosocial health of older people in China. This is a joint effort of 15 research centers located in the eastern, middle, and western parts of China, and samples were randomly selected from all permanent residents aged over 60 in the 2010 national census. It comprises 75 preclinical AD subjects who self-report having significant cognitive decline (SCD) at baseline. To be noted, SCD generally refers to the same disease stage as SMC, with slight differences in diagnostic standards [49, 50]. Based on a 7-year longitudinal follow-up, 51 subjects retained SCD status, and thus, are classified as stable SCD (sSCD). The remaining 24 subjects progress to MCI and are identified as progressive SCD (pSCD). The CLAS dataset exclusively contains baseline T1-weighted MRI data but lacks PET data.

3) **AIBL**. The AIBL provides both MRI and PET images from multiple sites. With the development of amyloid PET radiotracers, the study updates the radiotracers multiple times throughout their longitudinal study, providing PET images of three types of radiotracers, namely Pittsburgh Compound-B (PiB), ^{18}F -flutemetamol (FLUTE), and Flortbetapir (AV45). In this work, we employ the paired baseline amyloid PET and T1-weighted MRI from 331 CN subjects. As detailed in Table 1, these subjects are divided into three groups based on PET radiotracers, including 119 subjects with PiB-PET, 143 subjects with FLUTE-PET, and 69 subjects with AV45-PET. We manually exclude the scans that fail during preprocessing or exhibit significantly low image quality. Subject IDs are listed in the *Supplementary Materials*.

Image Processing. We utilize a standardized processing pipeline to unify images across all datasets. For 3D MRI scans, we apply skull stripping to each brain, normalize image intensity, and then register the brain to the MNI space. For 3D PET scans, we first apply skull stripping, then linearly align each PET to its paired MRI, and finally register the linearly aligned PET to MNI space with the deformation matrix created by MRI registration. All MRI and PET scans are uniformly cropped from the original dimensions (*i.e.*, $181 \times 217 \times 181$ with voxel dimensions of $1 \times 1 \times 1$) to the dimensions of $160 \times 180 \times 160$, to discard the uninformative background while still keep the whole brain. The image intensity is normalized to $[-1, 1]$ in the training phase, and $[0, 1]$ for computing the quantitative results.

4.2 Competing Methods

We compare the proposed FICD with six state-of-the-art 3D deep generative methods, including two GAN-based models, two VAE-based models, and two diffusion models.

1) **GAN**: The architecture of GAN contains a generator and a discriminator. The generator has a 3-layer encoder (with convolutional channel numbers of 16, 32, and 64), six

residual blocks, and a 2-layer decoder (with deconvolutional channel numbers of 32 and 16), followed by a final convolutional layer. The filter sizes for the first and last layers in the generator are set at $7 \times 7 \times 7$, while all other convolutional and deconvolutional layers use the filter size of $3 \times 3 \times 3$. The discriminator is equipped with five convolutional layers, progressively increasing in channel numbers from 32, 64, 128, to 256, and 1 channel for final output.

2) **CycleGAN**: This model includes two generators and two adversarial discriminators that form two branches for MRI to PET and PET to MRI prediction. The generator has a 3-layer encoder (with convolutional channel numbers of 8, 16, and 32), six residual blocks, and a 2-layer decoder (with deconvolutional channel numbers of 16 and 8), followed by a final convolutional layer. The filter sizes for the first and last layers in the generator are set at $7 \times 7 \times 7$, while all other convolutional and deconvolutional layers utilize a filter size of $3 \times 3 \times 3$. The discriminator is equipped with five convolutional layers, progressively increasing in channel numbers from 16, 32, 64, to 128, and 1 channel for final output. We leverage the publicly available pretrained CycleGAN [51] that translates between MRI and PET images.

3) **VAE**: The VAE is structured around two primary components: an encoder and a decoder. The encoder is built from five convolutional blocks, with the channel numbers increasing from 16 to 256, and with the feature map size progressively decreasing. Following each convolutional block is a residual block. The encoder’s output is then directed through two separate linear layers for computing the mean and variance. These are utilized for calculating the Kullback-Leibler divergence and shaping the distribution that serves as input to the decoder. Mirroring the encoder, the decoder features a symmetrical architecture but in reverse order, reconstructing the input data from the latent space representations generated by the encoder.

4) **VAEGAN**: The VAEGAN [37] integrates a VAE as the generator, alongside a discriminator for adversarial training. Due to computational power limitation, the channel numbers for this model are half of that in VAE, *i.e.*, 8, 16, 32, 64, and 128. The discriminator has four convolutional layers, with channel numbers 8, 16, 32, and 1 for label prediction.

5) **DDPM**: The DDPM [20] contains a forward diffusion process based on a Markov chain and learns the reverse denoising process. Similar to our method, MRI is used as the condition in this model. The DDPM can be treated as a vanilla framework of our proposed method. It shares a similar foundational structure with our FICD while only the noise-level constraint is utilized in the training phase. To ensure a fair comparison, we maintain identical hyperparameters, model structures, and Monte-Carlo sampling times in the diffusion-based models as those used in our framework’s training throughout all the experiments.

6) **LDM**: This method is based on the latent diffusion model (LDM) introduced in [52], which includes an encoder for feature extraction from images, a decoder for image reconstruction, and a denoising diffusion model for modality translation within the latent space. Initially, the encoder and decoder are trained jointly across 100 epochs to reconstruct PET images, utilizing the entire set of PET images in the training dataset. We then use the locked weights of the encoder to extract features from PET and MRI. Afterward,

we utilize the denoising diffusion model to convert MRI latent features into PET latent features, and the decoder, with its weights fixed as well, is applied to reconstruct the synthesized PET images. The Monte-Carlo sampling time here is also the same as FICD and DDPM.

4.3 Experimental Settings

Four tasks are performed in the experiments: 1) image synthesis, 2) disease progression forecasting, 3) prediction of future cognitive function, and 4) generalization evaluation. For Task 1, we train the proposed FICD and competing methods on ADNI CN subjects, and evaluate their performance in generating FDG-PET images with ground-truth scans available. For Task 2 and Task 3, we first use the models trained in Task 1 to synthesize missing PET data for ADNI and CLAS, and then perform downstream prediction. For Task 4, we use the AIBL data, where amyloid PET scans with three radiotracers (*i.e.*, PiB, FLUTE, and AV45) are available. Subject IDs can be found in Tables S1-S3 of *Supplementary Materials* to facilitate reproducible research.

Task 1: Image Synthesis. To assess the quality of the synthesized image, a total of 293 CN subjects with paired T1-weighted MRI and FDG-PET from ADNI are used in this task, as indicated in Table 1. Specifically, 263 subjects are used for model training, while the rest 30 subjects are used for testing. For diffusion models (*i.e.*, DDPM, LDM, and FICD), the outputs are the average of 10 times using MC sampling strategy. We use four evaluation metrics to assess the image quality at the 3D volume level, including 1) peak signal-to-noise ratio (PSNR), 2) structural similarity index measure (SSIM), 3) mean absolute error (MAE), and 4) normalized mutual information (NMI). For evaluation, the synthesized images are padded to their original size.

Task 2: Disease Progression Forecasting. This task aims to assess how effectively synthesized PET scans from a generative model can aid in training a downstream model for predicting the progression of preclinical AD. We deploy the trained FICD and each competing method from Task 1 to synthesize the missing PET for 119 AD subjects and 143 CN subjects from the ADNI dataset, as well as for all the subjects from the CLAS dataset. Given the time-consuming nature of the process, we apply Monte-Carlo with a sampling time of five for the diffusion-based models (*i.e.*, DDPM, LDM, and FICD) for this task and all subsequent ones. Following this, a classification model is trained on all available MRI and PET pairs, including both real and synthesized PET, to identify AD patients from CN. The classification model incorporates a dual-branch convolutional neural network (CNN) architecture with two branches of identical encoders for each modality. The features extracted from these encoders are then concatenated and subsequently fused in a transformer self-attention module [44] for final result prediction. Driven by the challenge of limited sample sizes in preclinical AD-related research [43, 46], the model (trained for AD vs. CN classification) is then used to classify between progressive and stable preclinical AD in a transfer learning manner. Two preclinical AD datasets are used: 1) SMC subjects from ADNI (denoted as ADNI-SMC), who have both modalities data, and 2) SCD subjects from CLAS (denoted as CLAS-SCD), which only has MRI data and has PET data synthesized by each method. We repeat the training phase for

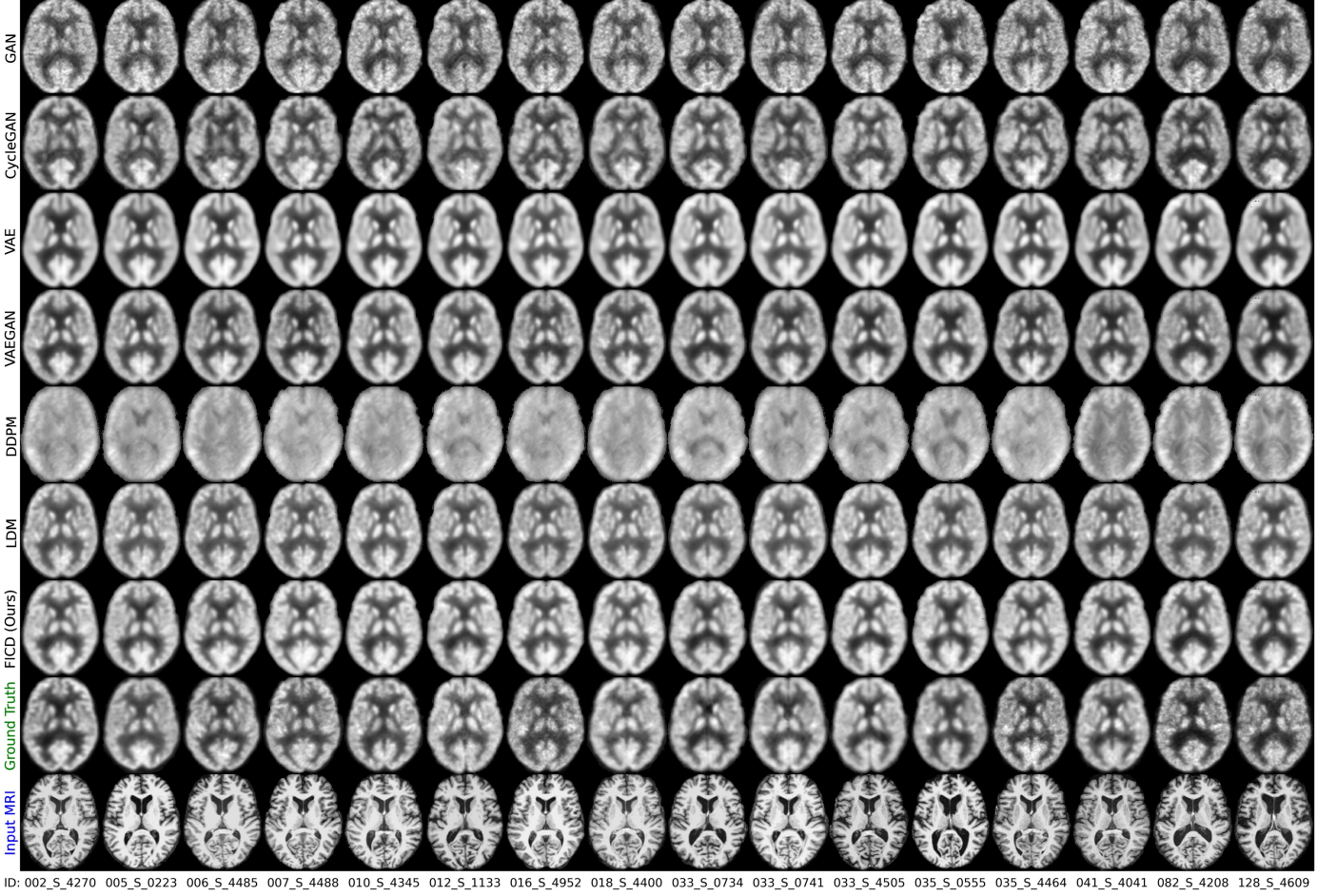


Fig. 3. Visualization of PET images synthesized by the proposed FICD and six competing methods on cognitively normal subjects from the test set in ADNI [43]. The ground-truth PET images and input MRI are displayed at the bottom with the corresponding subject ID.

this classification model five times with different random parameter initializations and record the mean and standard deviation results. Six evaluation metrics are used in this task, including area under the ROC curve (AUC), accuracy (ACC), sensitivity (SEN), specificity (SPE), balanced accuracy (BAC), and F1-Score (F1s).

Task 3: Prediction of Future Cognitive Function. Minimal state examination (MMSE) and clinical dementia rating (CDR) are pivotal tools in the evaluation of cognitive function and are instrumental in diagnosing and tracking the progression of neurodegenerative diseases, including Alzheimer’s disease and other forms of dementia [46, 53, 54]. Therefore, in this work, we include the task of predicting the future MMSE and CDR scores for preclinical AD subjects based on baseline MRI and PET. Specifically, for the ADNI-SMC cohort, we focus on predicting cognitive scores at 2-year follow-up, with 58 subjects having MMSE scores available (18 classified as pSMC and 40 classified as sSMC) and 17 subjects have CDR scores available (11 classified as pSMC and 6 classified as sSMC). For the CLAS-SCD cohort, all the subjects have MMSE scores available and have no CDR scores. We employ the same model structure as Task 2 with the output layer modified for linear regression to predict each type of cognitive score. The training phase for this prediction model is repeated five times with different random initializations. The outcomes of

TABLE 2
Quantitative evaluation results achieved by the proposed FICD and six competing methods for FDG-PET generation on ADNI, with best results shown in bold.

Method	PSNR↑	SSIM↑	MAE↓	NMI↑
GAN	24.3918±0.4501	0.8279±0.0001	0.0252±0.0022	0.7313±0.0208
CycleGAN	25.0409±1.0553	0.8691±0.0005	0.0236±0.0031	0.7490±0.0278
VAE	26.6605±0.8572	0.8838±0.0007	0.0195±0.0022	0.7944±0.0329
VAEGAN	26.8577±0.7049	0.8821±0.0005	0.0191±0.0021	0.8044±0.0243
LDM	26.3088±0.9892	0.8770±0.0215	0.0206±0.0026	0.8008±0.0287
DDPM	21.6955±0.6776	0.8319±0.0290	0.0367±0.0030	0.6929±0.0218
FICD (Ours)	27.8847±1.1676	0.9124±0.0239	0.0173±0.0026	0.8603±0.0355

these repeated training are then averaged, and we assess the model’s predictive accuracy by calculating the correlation coefficient (CC), root mean squared error (RMSE), and mean absolute error (MAE) between the predicted and real scores.

Task 4: Generalization Evaluation. Amyloid PET which shows brain amyloid deposition is another pivotal molecular imaging biomarker for the investigation of dementia, providing complementary information for FDG-PET that measures regional glucose consumption [24]. Therefore, we extend the application of the proposed FICD to encompass the synthesis of amyloid PET images associated with several commonly employed radiotracers (*i.e.*, PiB, FLUTE, and AV45). Specifically, for each type of radiotracer, we fine-tune the FICD model—initially pre-trained on FDG-PET data from the ADNI—for 7 epochs, using MRI inputs to generate amyloid PET images. Same as the settings in FDG-

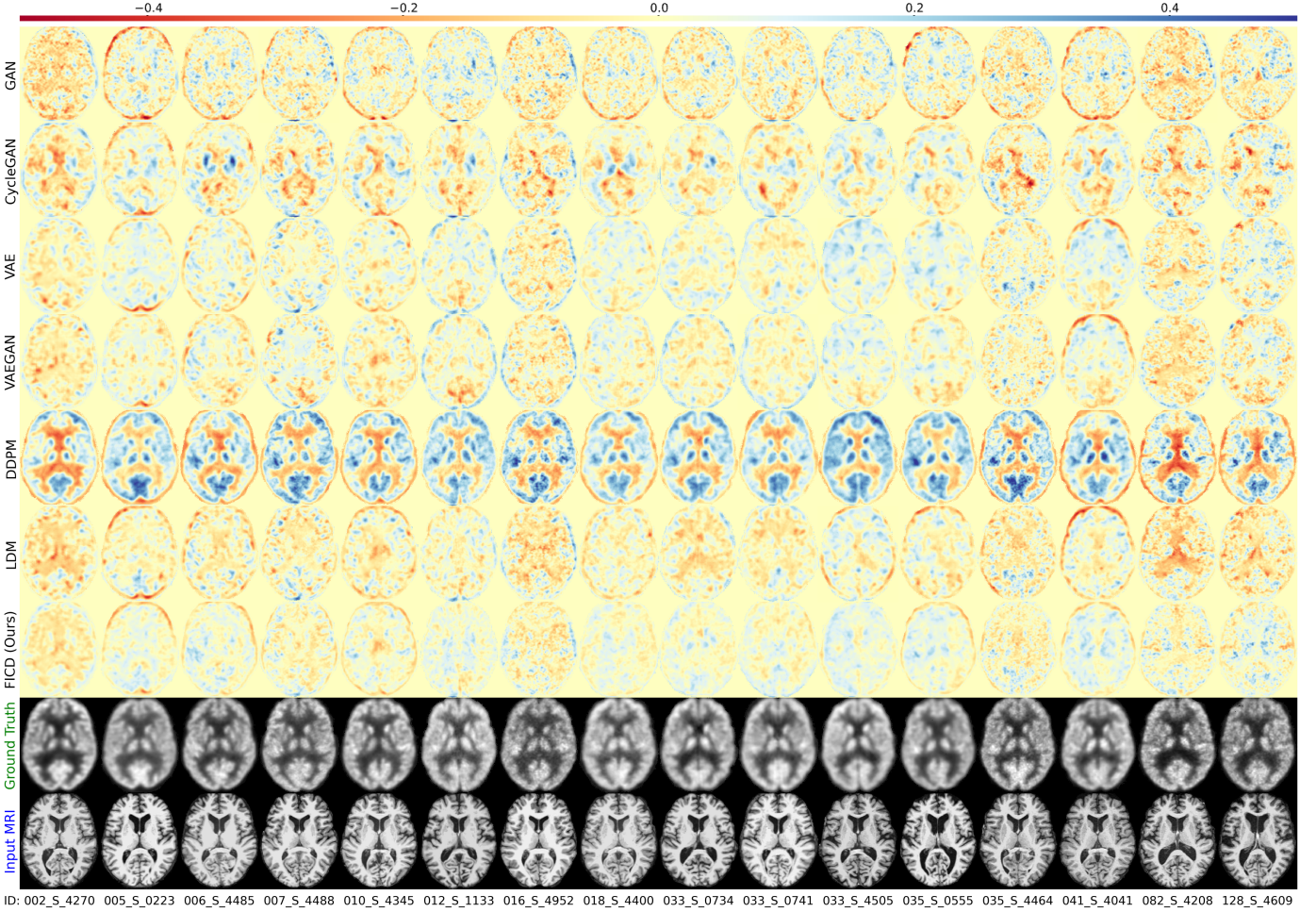


Fig. 4. Difference maps for synthetic PET images generated by the proposed FICD and six competing methods on cognitively normal subjects from the test set in ADNI [43]. The ground-truth PET images and input MRI are displayed at the bottom with the corresponding subject ID.

TABLE 3

Results (mean±standard deviation) of different methods in the tasks of CLAS-SCD progression prediction (*i.e.*, pSCD vs. sSCD classification) and ADNI-SMC progression prediction (*i.e.*, pSMC vs. sSMC classification) with the input of PET and MRI scans.

Method	pSCD vs. sSCD classification on CLAS-SCD						pSMC vs. sSMC classification on ADNI-SMC					
	AUC (%)↑	ACC (%)↑	SEN (%)↑	SPE (%)↑	BAC (%)↑	F1s (%)↑	AUC (%)↑	ACC (%)↑	SEN (%)↑	SPE (%)↑	BAC (%)↑	F1s (%)↑
GAN	60.89±7.62	58.13±4.59	61.67±7.17	56.47±3.37	59.07±5.27	48.52±5.64	67.12±7.33	60.33±4.91	65.26±7.88	58.10±3.56	61.68±5.72	50.61±6.11
CycleGAN	57.11±3.27	55.47±2.00	57.50±3.12	54.51±1.47	56.00±2.29	45.25±2.45	66.89±2.30	58.36±2.45	62.11±3.94	56.67±1.78	59.39±2.86	48.16±3.05
VAE	56.62±5.00	52.80±3.11	53.33±4.86	52.55±2.29	52.94±3.57	41.97±3.82	63.66±7.69	60.33±5.33	65.26±8.55	58.10±3.87	61.68±6.21	50.61±6.63
VAEGAN	57.22±5.93	54.40±2.72	55.83±4.25	53.73±2.00	54.78±3.12	43.93±3.34	67.89±4.57	59.02±2.07	63.16±3.33	57.14±1.51	60.15±2.42	48.98±2.58
DDPM	53.64±5.64	51.73±3.62	51.67±5.65	51.76±2.66	51.72±4.16	40.66±4.45	65.99±5.33	59.67±3.21	64.21±5.16	57.62±2.33	60.91±3.74	49.80±4.00
LDM	57.17±4.32	56.00±4.46	58.33±6.97	54.90±3.28	56.62±5.13	45.90±5.49	68.80±5.52	61.64±6.36	67.37±10.21	59.05±4.62	63.21±7.41	52.24±7.91
FICD (Ours)	63.77±2.72	58.67±2.39	62.50±3.73	56.86±1.75	59.68±2.74	49.18±2.93	72.78±2.83	63.61±2.62	70.53±4.21	60.48±1.90	65.50±3.06	54.69±3.27

PET synthesis in Task 1, the AIBL data is partitioned into 90% for fine-tuning and 10% for test, with the detailed subject number of each radiotracer reported in Table 1.

4.4 Results of Image Synthesis

4.4.1 Quantitative Results

Table 2 shows the quantitative results of our proposed FICD with six other competing methods. The results illustrate that FICD outperforms all other methods across every evaluation metric. Notably, compared to DDPM, our method enhances the PSNR by nearly 30% and reduces the MAE by more than half. These improvements underscore the significant impact of the introduced functional imaging constraint in

improving the accuracy of the synthesized images. Additionally, LDM is inferior to our FICD, which may be due to potential information loss during its encoding process that maps images into low-dimensional latent space. Both VAE-based methods (*i.e.*, VAE and VAEGAN) produce PET images that yield satisfactory quantitative results, surpassing both GAN-based methods (*i.e.*, GAN and CycleGAN) and diffusion-based competing methods (*i.e.*, DDPM and LDM). Among the GAN-based methods, CycleGAN achieves better results than GAN across all evaluation metrics.

4.4.2 Qualitative Results

Figure 3 compares the axial slices of PET images synthesized by the FICD and six other methods, with the last two rows

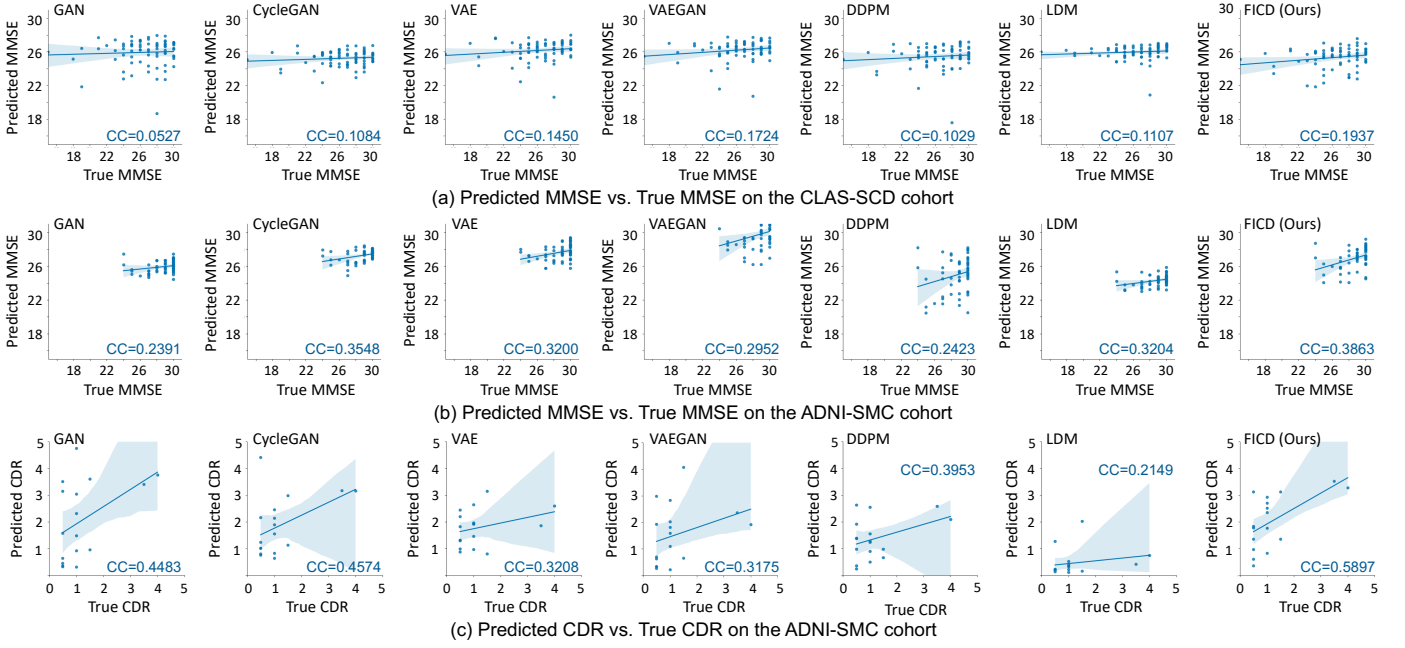


Fig. 5. Scatter diagrams of cognitive scores (i.e., MMSE and CDR) predicted by different methods for CLAS-SCD at 7-year follow-up and ADNI-SMC at 2-year follow-up, with baseline images as input. CC: correlation coefficient; MMSE: mini-mental state examination; CDR: clinical dementia rating.

TABLE 4

Results of different methods in cognitive function prediction for CLAS-SCD at 7-year follow-up and ADNI-SMC at 2-year follow-up, with the baseline imaging data as input.

Method	MMSE of CLAS-SCD			MMSE of ADNI-SMC			CDR of ADNI-SMC		
	CC \uparrow	RMSE \downarrow	MAE \downarrow	CC \uparrow	RMSE \downarrow	MAE \downarrow	CC \uparrow	RMSE \downarrow	MAE \downarrow
GAN	0.0527	3.4817	2.7573	0.2391	3.2200	2.9941	0.4483	1.5876	1.0944
CycleGAN	0.1084	3.3857	2.7751	0.3548	2.1290	1.9563	0.4574	1.2650	0.9123
VAE	0.1450	3.1875	2.4738	0.3200	1.1921	1.6664	0.3208	1.0339	0.8554
VAEGAN	0.1724	3.1571	2.4230	0.2952	2.2013	1.6909	0.3175	1.2697	0.9756
DDPM	0.1029	3.4389	2.7417	0.2423	4.3843	3.9687	0.3953	1.0012	0.8014
LDM	0.1107	3.1838	2.4991	0.3204	4.6849	4.4609	0.2149	1.2404	0.872
FICD (Ours)	0.1937	3.3258	2.7092	0.3863	2.4238	2.0940	0.5897	1.2320	0.9852

showing the ground-truth PET and input MRI, respectively. We further show the difference maps of each synthetic PET image in Fig. 4, which are generated by calculating the difference between a synthetic PET and its ground truth. Visualizations of these images from the sagittal and coronal planes are available in *Supplementary Material*. From Fig. 3, we can observe that the PET images generated by FICD are distinguished by their superior quality and similarity to the ground truth. This is particularly evident in gray matter regions, including the *temporal lobes*, *precuneus*, and *parietal cortex*. These regions exhibit typical patterns of hypometabolism associated with Alzheimer’s disease, and thus, accurate representation of these regions is essential for early detection and diagnosis [24, 55, 56].

The PET images synthesized by GAN and CycleGAN exhibit good similarity to the ground truth but with more noticeable noise. Besides, the images synthesized by VAE and VAEGAN generally show limited diversity, indicating a relatively uniform output regardless of variations in the input, compared with other methods. This uniformity can often be attributed to a weak association between the posterior distribution and the model input, a phenomenon frequently encountered in VAE [18]. This may prevent the model from

TABLE 5

Results of fine-tuning the proposed FICD to synthesize PET images of different radiotracers from the AIBL cohort.

Radiotracer	PSNR \uparrow	SSIM \uparrow	MAE \downarrow	NMI \uparrow
AV45	22.8995 \pm 2.7352	0.8527 \pm 0.0643	0.0319 \pm 0.0102	0.7335 \pm 0.0861
PiB	21.4160 \pm 0.9953	0.8093 \pm 0.0096	0.0366 \pm 0.0069	0.7174 \pm 0.0107
FLUTE	26.9723 \pm 1.6334	0.9089 \pm 0.0148	0.0194 \pm 0.0040	0.8717 \pm 0.0542

recognizing and encoding the unique characteristics of individual subjects. As a result, while the model may achieve low quantitative errors, it lacks the specificity required for detailed analysis of individual disease cases, compromising its utility in personalized diagnostics. Besides, VAE-generated PET tends to be blurrier compared to those from other methods. Among various competing methods, LDM generates images of acceptable quality. However, it does not preserve image details as accurately as FICD. The DDPM produces images with brightness around the brain’s periphery but a diminished representation of the brain details. The synthesized output predominantly maintains the structure of the input MRI, resulting in what might be considered a PET-style MRI scan. This outcome might be attributed to the fact that ground-truth PET data is not included in model optimization, which also highlights the effectiveness of our functional imaging constraint in enhancing image fidelity in cross-modality data translation.

4.5 Results of Disease Progression Forecasting

The results of combining real and synthetic images for AD and CN subjects and transferring their categorical information to progressive SCD and stable SCD subjects are presented in Table 3. From the table, we have a few observations. First, the images synthesized by our proposed FICD demonstrate superior performance in classification tasks across both datasets, outperforming other methods across all evaluation metrics. These results indicate that the

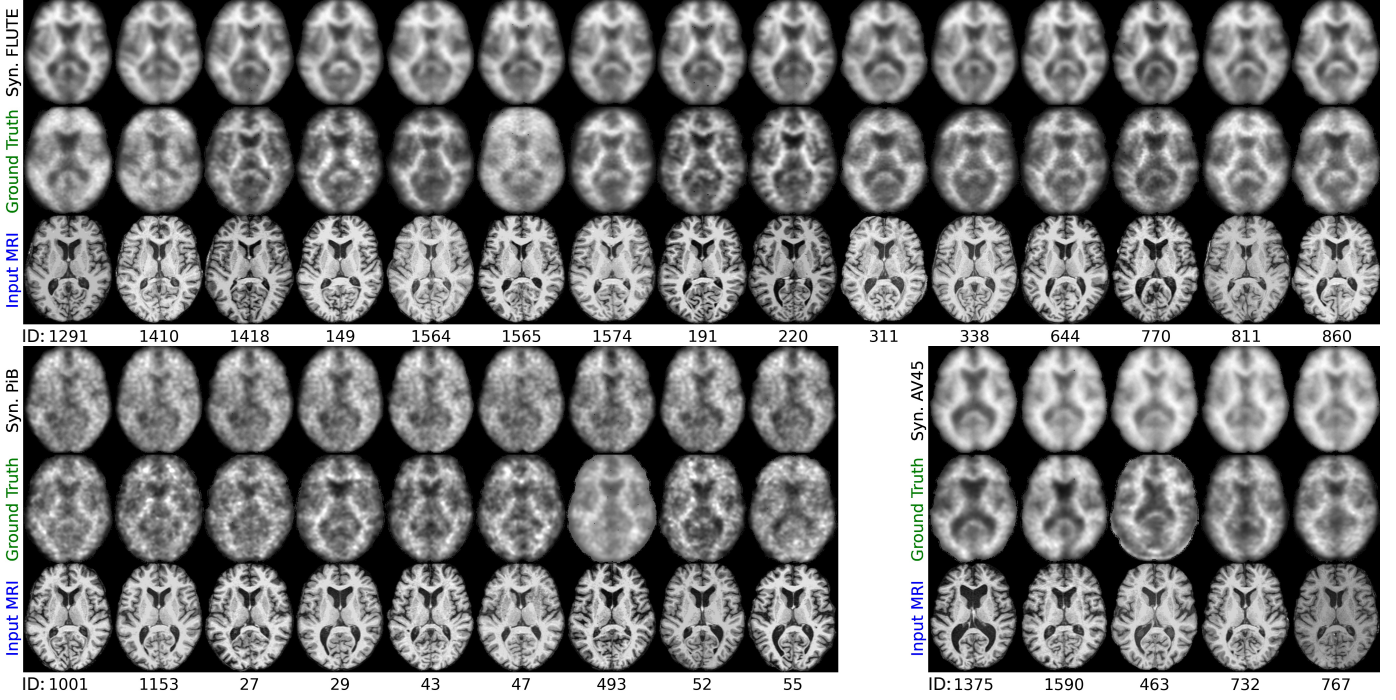


Fig. 6. Visualization of synthesized PET images using the FICD for three different amyloid PET tracers: FLUTE (top), PiB (bottom left), and AV45 (bottom right), compared with the ground-truth PET images and the corresponding input MRI scans from AIBL [47].

images synthesized by FICD more effectively capture AD-specific features critical for analyzing AD-related diseases.

The GAN-based methods deliver generally higher results compared with VAE, although they achieve lower quantitative results. These results align with observations noted in the qualitative results section that GAN-based results can also capture good brain details, although the GAN-generated images are prone to noise. In contrast, VAE performs less effectively in both tasks, as the synthesized images lack sufficient discriminative information for prediction. On the other hand, VAEGAN and LDM produce comparable results, consistent with their quantitative performance. DDPM, however, shows lower efficacy in these tasks. Notably, the classification between pSMC and sSMC in ADNI-SMC yields higher results across all synthesizing methods than that of pSCD vs. sSCD classification on CLAS, which could be attributed to less domain gap between the test data and training data since they all come from ADNI.

4.6 Results of Future Cognitive Function Prediction

In this group of experiments, we aim to predict future brain cognitive function based on baseline MRI and PET, where missing PET images are imputed through a specific method. Table 4 shows the prediction results of two cognitive scores and Fig. 5 shows the scatter plot of the results. From these results, we can observe that the cognitive scores predicted by FICD have the highest correlation with the ground truth, on two types of clinical scores (*i.e.*, MMSE and CDR) and two sources of datasets (*i.e.*, CLAS-SCD and ADNI-SMC). These results indicate that PET images synthesized by FICD produce the best results in predicting future brain cognitive function using baseline neuroimaging data.

4.7 Results of Generalization Evaluation

4.7.1 Quantitative Results

Table 5 presents the quantitative results of applying FICD to amyloid PET in AIBL with three radiotracers. Note that FICD is initially trained on FDG-PET images from ADNI and fine-tuned for each radiotracer. Among them, FLUTE-PET achieves impressive results, closely paralleling those obtained with FDG-PET. The outcomes for PiB-PET and AV45-PET are relatively lower, which may be attributed to less training data and inconsistencies in image quality across different subjects in the original datasets.

4.7.2 Qualitative Results

Figure 6 shows the qualitative result of PET with the three tracers. Aligning with previous quantitative results, FLUTE-PET scans are synthesized with very high fidelity. The PiB-PET scans are not as smooth as FLUTE-PET, which is caused by the radiotracer’s characteristic that ^{11}C for PiB-PET has a short radioactive decay half-life (20 minutes) [57]. This introduces a degree of unpredictability to the images. Despite this, both synthesized PiB-PET and AV45-PET scans effectively capture detailed functional information. To be noted, while the synthesized images consistently maintain uniform quality, there is noticeable variability in the quality of ground-truth PET images from AIBL.

5 DISCUSSION

5.1 Influence of Functional Imaging Constraint

We further investigate the influence of the proposed functional imaging constraint by comparing the training efficiency of DDPM and our FICD. According to Eqs. (8)-(11), the accurate estimate of X^0 (*i.e.* \tilde{X}^0) is essential as it influences the inference process to get X^{t-1} . During each

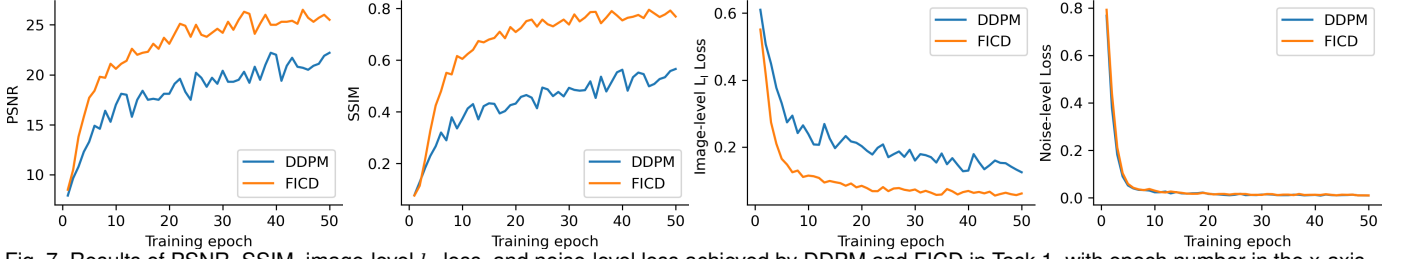


Fig. 7. Results of PSNR, SSIM, image-level l_1 loss, and noise-level loss achieved by DDPM and FICD in Task 1, with epoch number in the x-axis.

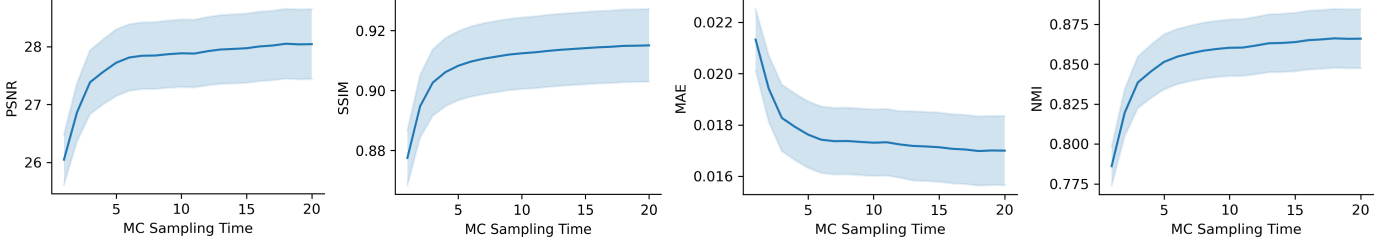


Fig. 8. Quantitative results achieved by FICD using different Monte-Carlo (MC) sampling times in Task 1.

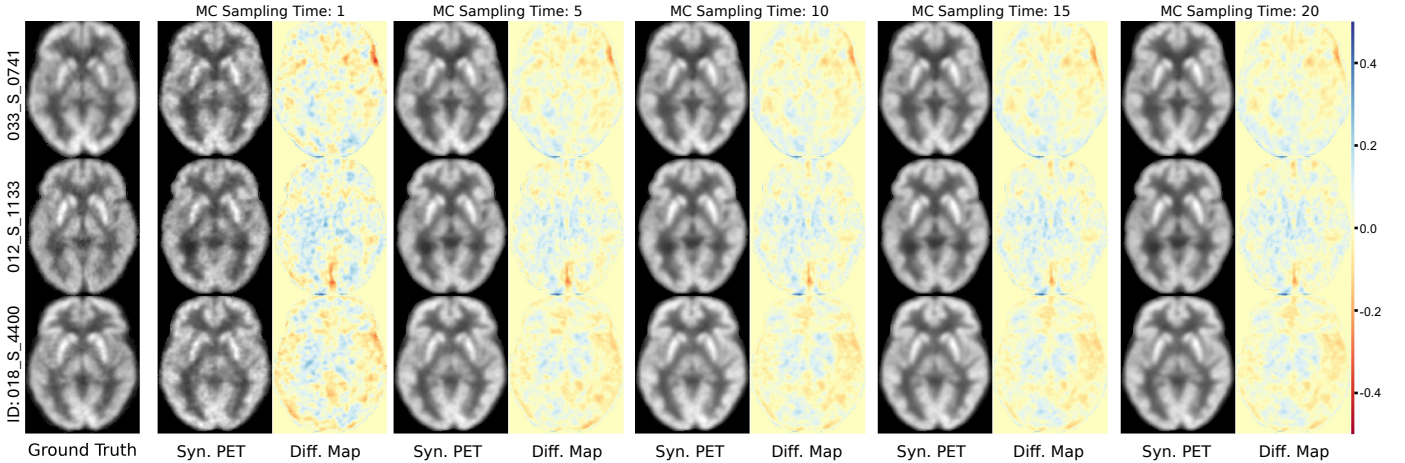


Fig. 9. Synthesized (Syn.) PET images and difference (Diff.) maps achieved by FICD using varying Monte-Carlo (MC) sampling times, with ground-truth PET images from ADNI [43] shown on the left for comparison.

training epoch, we calculate \tilde{X}^0 using Eq. (5) and compare it with the ground truth. The comparison is evaluated through PSNR, SSIM, and image-level l_1 loss defined in Eq. (6). The noise-level loss in Eq. (4) of both methods is also recorded. Since DDPM does not employ a functional imaging constraint in training, we compute the l_1 loss between its \tilde{X}^0 and the ground truth for comparing purposes only.

Figure 7 depicts the trends in PSNR, SSIM, image-level l_1 loss, and noise-level loss throughout the training epochs for FICD and DDPM. From this figure, we can observe that even though the two methods have similar converging speeds in terms of noise-level loss, their corresponding \tilde{X}^0 have distinct results indicated by PSNR, SSIM, and image-level l_1 loss. The FICD shows rapid convergence in metrics evaluating \tilde{X}^0 , whereas DDPM’s convergence is significantly slower and yields less favorable outcomes. The findings indicate that in the absence of a functional imaging constraint, the denoising diffusion model struggles to produce high-quality images.

On the other hand, in Figure 2, we present the outcomes of DDPM and FICD using different instances of random Gaussian noise. The DDPM outputs displayed in Fig. 2 (a)

show significant variability among the different samplings, in contrast to the more consistent results of FICD shown in Fig. 2 (b). These results further suggest the benefit of integrating a functional imaging constraint within a diffusion model (as we do in FICD), which not only improves the fidelity of synthesized images but also significantly reduces the variability in outputs, leading to more stable results.

5.2 Analysis of Model Variability in Inference

As described in Section 3, the input for the inference phase is a random noise concatenated with MRI, and the random noise is updated in each timestep to generate corresponding PET, leading to a slight difference in synthesized images. Following [41], we incorporate Monte-Carlo (MC) sampling into our framework to mitigate this issue. We further investigate the influence of varying MC sampling times on the final synthesized PET in Task 1. The quantitative outcomes of this analysis are presented in Fig. 8, which shows a significant enhancement in terms of image quality as the MC sampling times are elevated from 1 to 5. Beyond a sampling time of 5, the performance enhancements from additional sampling become marginal. Figure 9 provides a visual comparison of

TABLE 6

Results of preclinical AD progression prediction on subjects from two preclinical AD datasets, with different imaging modalities at baseline as input.

Modality	Training Subject #	pSCD vs. sSCD classification on CLAS						pSMC vs. sSMC classification on ADNI					
		AUC (%)↑	ACC (%)↑	SEN (%)↑	SPE (%)↑	BAC (%)↑	F1s (%)↑	AUC (%)↑	ACC (%)↑	SEN (%)↑	SPE (%)↑	BAC (%)↑	F1s (%)↑
MRI only	795	56.42±4.04	51.20±4.27	50.83±6.67	51.37±3.14	51.10±4.90	40.00±5.25	68.92±4.28	59.02±3.59	63.16±5.77	57.14±2.61	60.15±4.19	48.98±4.47
MRI+Real PET	533	53.12±3.55	50.67±2.92	50.00±4.56	50.98±2.15	50.49±3.36	39.34±3.59	68.70±5.75	60.98±4.45	66.32±7.14	58.57±3.23	62.44±5.18	51.43±5.45
FICD (Ours)	795	63.77±2.72	58.67±2.39	62.50±3.73	56.86±1.75	59.68±2.74	49.18±2.93	72.78±2.83	63.61±2.62	70.53±4.21	60.48±1.90	65.50±3.06	54.69±3.27

TABLE 7

Quantitative evaluation results of synthetic PET images generated by the proposed FICD using MRI gradient maps and MRI scans as conditions, with best results shown in bold.

Condition	PSNR↑	SSIM↑	MAE↓	NMI↑
Gradient	26.7001±0.8556	0.9018±0.0222	0.0199±0.0021	0.8333±0.0304
MRI	27.7210±1.1552	0.9083±0.0231	0.0176±0.0026	0.8514±0.0347

synthesized images produced at MC sampling times from 1 to 20. From this figure, we can observe that with the increase in sampling times, the images gradually become smoother and the difference between a synthetic PET and its ground truth tends to be smaller, indicating an enhancement in image quality. When the MC sampling time is greater than 5, one can obtain a very stable output image with only a limited improvement in image quality. Considering the time-consuming nature of the inference phase, it becomes crucial to balance the benefits of increased sampling times against the associated computational costs.

5.3 Influence of PET Imputation

We further investigate the influence of PET imputation on downstream tasks by examining Task 2 outcomes across three scenarios: 1) MRI only: when the subjects of the entire cohort have only MRI data, 2) MRI+Real PET: when two modalities are used but only a subset of the entire cohort has paired real MRI and PET images available, and 3) FICD: when the entire cohort has paired multimodal images, with the missing PET synthesized by FICD. The results presented in Table 6 indicate that the highest accuracy is achieved when synthesized images are used to complete the modalities for all cohorts, significantly outperforming other scenarios. In cases where only real MRI and PET are utilized, the performance is not good, which may be attributed to the limited sample size (*i.e.*, only 533 subjects). When only using MRI, there’s a marginal increase in results, however, these outcomes don’t reach the enhanced performance levels achieved by our approach with synthesized PET images.

5.4 Influence of Input Condition

We also investigate the influence of conditional inputs on the proposed FICD. As mentioned in Section 3, in addition to MRI, we can also apply the gradient of MRI as a condition to FICD. Here, we compare the influence of these two types of conditions used in FICD and perform image synthesis (same in Task 1). The quantitative evaluation results are reported in Table 7. All the experimental settings remain consistent across both methods, and evaluations are conducted with an MC sampling time of 5. From Table 7, utilizing MRI directly as the condition yields marginally better results. The

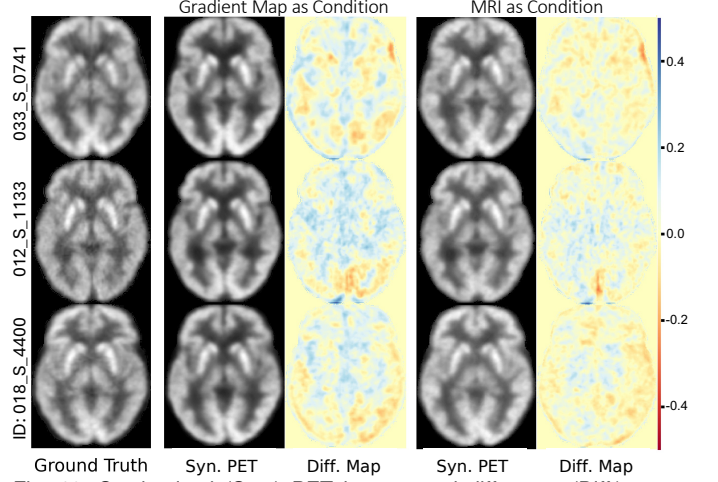


Fig. 10. Synthesized (Syn.) PET images and difference (Diff.) maps achieved by FICD using MRI gradient map and MRI as the condition, with ground truth from ADNI [43] shown on the left for comparison.

results with the gradient of MRI as a condition are also noteworthy and present a viable alternative to condition FICD. Figure 10 compares the output of FICD using MRI gradient map versus MRI as the condition. Both results provide clear brain functional information closely resembling the ground truth, while the gradient map-conditioned results show greater image contrast.

5.5 Limitations and Future Work

Some limitations of the current study should be noted. *On one hand*, in this work, the FICD is trained exclusively on cognitively normal subjects and is utilized to synthesize PET images across various disease categories. This may constrain the model’s effectiveness, potentially overlooking subtle disease-specific brain pathology. As a future work, we could broaden its learning scope by including data with different brain states. This could be achieved by integrating disease-related information through category labels, or by just inputting data spanning all categories to capture a wider spectrum of disease-specific features. *On the other hand*, another notable challenge is the extensive training time required by the current model. On an RTX 3090 GPU with 24 GB memory, the FICD takes around 3 hours to train one epoch, and around 10 minutes to infer one image with 1,000 timesteps. Future enhancements could involve the integration of denoising diffusion implicit models [58], which could significantly accelerate the inference phase. This adjustment would improve the model’s efficiency and make it more feasible for broader applications.

6 CONCLUSION

This paper introduces a functional imaging constrained diffusion (FICD) framework for 3D brain PET image synthesis from structural MRI through a new constrained diffusion model (CDM). The FICD achieves stable training by progressively adding random noise to PET images and eventually removing noise via CDM. Incorporated with a functional imaging constraint that ensures voxel-wise accuracy relative to ground-truth PET, CDM learns to predict scheduled noise added to PET. Quantitative and qualitative evaluations on a dataset of 293 subjects with paired T1-weighted MRI and FDG-PET have demonstrated that FICD outperforms existing state-of-the-art methods. Further validation on three downstream tasks for brain cognitive function prediction and amyloid PET synthesis is conveyed involving 1,262 subjects, with results suggesting the effectiveness and generalizability of the proposed framework.

ACKNOWLEDGMENTS

A part of the data used in this work is from the Alzheimer's Disease Neuroimaging Initiative (ADNI) and the Australian Imaging, Biomarkers and Lifestyle (AIBL). The ADNI and AIBL investigators provide the data but are not involved in the processing, analysis, and writing. A comprehensive list of ADNI investigators is accessible [online](#).

REFERENCES

- [1] B. H. Ridha, J. Barnes, J. W. Bartlett, A. Godbolt, T. Pepple, M. N. Rossor, and N. C. Fox, "Tracking atrophy progression in familial Alzheimer's disease: A serial MRI study," *The Lancet Neurology*, vol. 5, no. 10, pp. 828–834, 2006.
- [2] B. C. Dickerson, A. Bakkour, D. H. Salat, E. Feczko, J. Pacheco, D. N. Greve, F. Grodstein, C. I. Wright, D. Blacker, H. D. Rosas *et al.*, "The cortical signature of Alzheimer's disease: Regionally specific cortical thinning relates to symptom severity in very mild to mild AD dementia and is detectable in asymptomatic amyloid-positive individuals," *Cerebral Cortex*, vol. 19, no. 3, pp. 497–510, 2009.
- [3] C. Hohenfeld, C. J. Werner, and K. Reetz, "Resting-state connectivity in neurodegenerative disorders: Is there potential for an imaging biomarker?" *NeuroImage: Clinical*, vol. 18, pp. 849–870, 2018.
- [4] P. J. Nestor, D. Altomare, C. Festari, A. Drzezga, J. Rivolta, Z. Walker, F. Bouwman, S. Orini, I. Law, F. Agosta *et al.*, "Clinical utility of FDG-PET for the differential diagnosis among the main forms of dementia," *European Journal of Nuclear Medicine and Molecular Imaging*, vol. 45, pp. 1509–1525, 2018.
- [5] P. N. Young, M. Estarellas, E. Coomans, M. Srikrishna, H. Beaumont, A. Maass, A. V. Venkataraman, R. Lissaman, D. Jiménez, M. J. Betts *et al.*, "Imaging biomarkers in neurodegeneration: Current and future practices," *Alzheimer's Research & Therapy*, vol. 12, pp. 1–17, 2020.
- [6] C. Domínguez-Fernández, J. Egiguren-Ortiz, J. Razquin, M. Gómez-Galán, L. De las Heras-García, E. Paredes-Rodríguez, E. Astigarraga, C. Miguélez, and G. Barreda-Gómez, "Review of technological challenges in personalised medicine and early diagnosis of neurodegenerative disorders," *International Journal of Molecular Sciences*, vol. 24, no. 4, p. 3321, 2023.
- [7] C. Hinrichs, V. Singh, G. Xu, and S. C. Johnson, "Predictive markers for AD in a multi-modality framework: An analysis of MCI progression in the ADNI population," *NeuroImage*, vol. 55, no. 2, pp. 574–589, 2011.
- [8] I. M. Nasrallah and D. A. Wolk, "Multimodality imaging of Alzheimer's disease and other neurodegenerative dementias," *Journal of Nuclear Medicine*, vol. 55, no. 12, pp. 2003–2011, 2014.
- [9] R. Wittenberg, M. Knapp, M. Karagiannidou, J. Dickson, and J. M. Schott, "Economic impacts of introducing diagnostics for mild cognitive impairment Alzheimer's disease patients," *Alzheimer's & Dementia: Translational Research & Clinical Interventions*, vol. 5, pp. 382–387, 2019.
- [10] S. Sharma and P. K. Mandal, "A comprehensive report on machine learning-based early detection of Alzheimer's disease using multi-modal neuroimaging data," *ACM Computing Surveys*, vol. 55, no. 2, pp. 1–44, 2022.
- [11] Y. Pan, M. Liu, Y. Xia, and D. Shen, "Disease-image-specific learning for diagnosis-oriented neuroimage synthesis with incomplete multi-modality data," *IEEE Transactions on Pattern Analysis and Machine Intelligence*, vol. 44, no. 10, pp. 6839–6853, 2021.
- [12] S. Hu, B. Lei, S. Wang, Y. Wang, Z. Feng, and Y. Shen, "Bidirectional mapping generative adversarial networks for brain MR to PET synthesis," *IEEE Transactions on Medical Imaging*, vol. 41, no. 1, pp. 145–157, 2021.
- [13] J. Zhang, X. He, L. Qing, F. Gao, and B. Wang, "BPGAN: Brain PET synthesis from MRI using generative adversarial network for multi-modal Alzheimer's disease diagnosis," *Computer Methods and Programs in Biomedicine*, vol. 217, p. 106676, 2022.
- [14] F. Vega, A. Addeh, A. Ganesh, E. E. Smith, and M. E. MacDonald, "Image translation for estimating two-dimensional axial amyloid-beta PET from structural MRI," *Journal of Magnetic Resonance Imaging*, vol. 59, no. 3, pp. 1021–1031, 2024.
- [15] I. Goodfellow, "NIPS 2016 tutorial: Generative adversarial networks," *arXiv preprint arXiv:1701.00160*, 2016.
- [16] F. Li, W. Huang, M. Luo, P. Zhang, and Y. Zha, "A new VAE-GAN model to synthesize arterial spin labeling images from structural MRI," *Displays*, vol. 70, p. 102079, 2021.
- [17] H. Yang, X. Lu, S.-H. Wang, Z. Lu, J. Yao, Y. Jiang, and P. Qian, "Synthesizing multi-contrast MR images via novel 3D conditional variational auto-encoding GAN," *Mobile Networks and Applications*, vol. 26, pp. 415–424, 2021.
- [18] J. Lucas, G. Tucker, R. B. Grosse, and M. Norouzi, "Don't blame the ELBO! a linear VAE perspective on posterior collapse," *Advances in Neural Information Processing Systems*, vol. 32, 2019.
- [19] J. Sohl-Dickstein, E. Weiss, N. Maheswaranathan, and S. Ganguli, "Deep unsupervised learning using nonequilibrium thermodynamics," in *International Conference on Machine Learning*. PMLR, 2015, pp. 2256–2265.
- [20] J. Ho, A. Jain, and P. Abbeel, "Denoising diffusion probabilistic models," *Advances in Neural Information Processing Systems*, vol. 33, pp. 6840–6851, 2020.
- [21] P. Dhariwal and A. Nichol, "Diffusion models beat GANs on image synthesis," *Advances in Neural Information Processing Systems*, vol. 34, pp. 8780–8794, 2021.
- [22] H. Cao, C. Tan, Z. Gao, Y. Xu, G. Chen, P.-A. Heng, and S. Z. Li, "A survey on generative diffusion models," *IEEE Transactions on Knowledge and Data Engineering*, 2024.
- [23] A. Kazerouni, E. K. Aghdam, M. Heidari, R. Azad, M. Fayyaz, I. Hacihaliloglu, and D. Merhof, "Diffusion models in medical imaging: A comprehensive survey," *Medical Image Analysis*, p. 102846, 2023.
- [24] G. Chételat, J. Arbizu, H. Barthel, V. Garibotto, I. Law, S. Morbelli, E. van de Giessen, F. Agosta, F. Barkhof, D. J. Brooks *et al.*, "Amyloid-PET and 18F-FDG-PET in the diagnostic investigation of Alzheimer's disease and other dementias," *The Lancet Neurology*, vol. 19, no. 11, pp. 951–962, 2020.
- [25] M. W. Weiner, D. P. Veitch, P. S. Aisen, L. A. Beckett, N. J. Cairns, R. C. Green, D. Harvey, C. R. Jack, W. Jagust, E. Liu *et al.*, "The Alzheimer's Disease Neuroimaging Initiative: A review of papers published since its inception," *Alzheimer's & Dementia*, vol. 9, no. 5, pp. e111–e194, 2013.
- [26] R. J. Perrin, A. M. Fagan, and D. M. Holtzman, "Multimodal techniques for diagnosis and prognosis of Alzheimer's disease," *Nature*, vol. 461, no. 7266, pp. 916–922, 2009.
- [27] K. Walhovd, A. Fjell, A. Dale, L. McEvoy, J. Brewer, D. Karow, D. Salmon, and C. Fennema-Notestine, "Multi-modal imaging predicts memory performance in normal aging and cognitive decline," *Neurobiology of Aging*, vol. 31, no. 7, pp. 1107–1121, 2010.
- [28] C. R. Jack Jr, V. J. Lowe, M. L. Senjem, S. D. Weigand, B. J. Kemp, M. M. Shungu, D. S. Knopman, B. F. Boeve, W. E. Klunk, C. A. Mathis *et al.*, "¹¹C PiB and structural MRI provide complementary information in imaging of Alzheimer's disease and amnesic mild cognitive impairment," *Brain*, vol. 131, no. 3, pp. 665–680, 2008.
- [29] M. Abdelaziz, T. Wang, and A. Elazab, "Alzheimer's disease diagnosis framework from incomplete multimodal data using convolutional neural networks," *Journal of Biomedical Informatics*, vol. 121, p. 103863, 2021.

- [30] K. Ritter, J. Schumacher, M. Weygandt, R. Buchert, C. Allefeld, and J.-D. Haynes, "Multimodal prediction of conversion to Alzheimer's disease based on incomplete biomarkers," *Alzheimer's & Dementia: Diagnosis, Assessment & Disease Monitoring*, vol. 1, no. 2, pp. 206–215, 2015.
- [31] L. Yuan, Y. Wang, P. M. Thompson, V. A. Narayan, and J. Ye, "Multi-source feature learning for joint analysis of incomplete multiple heterogeneous neuroimaging data," *NeuroImage*, vol. 61, no. 3, pp. 622–632, 2012.
- [32] S. Xiang, L. Yuan, W. Fan, Y. Wang, P. M. Thompson, J. Ye, A. D. N. Initiative *et al.*, "Bi-level multi-source learning for heterogeneous block-wise missing data," *NeuroImage*, vol. 102, pp. 192–206, 2014.
- [33] T. Xie, C. Cao, Z. Cui, Y. Guo, C. Wu, X. Wang, Q. Li, Z. Hu, T. Sun, Z. Sang *et al.*, "Synthesizing PET images from high-field and ultra-high-field MR images using joint diffusion attention model," *arXiv preprint arXiv:2305.03901*, 2023.
- [34] I. Goodfellow, J. Pouget-Abadie, M. Mirza, B. Xu, D. Warde-Farley, S. Ozair, A. Courville, and Y. Bengio, "Generative adversarial networks," *Communications of the ACM*, vol. 63, no. 11, pp. 139–144, 2020.
- [35] O. Ronneberger, P. Fischer, and T. Brox, "U-Net: Convolutional networks for biomedical image segmentation," in *Medical Image Computing and Computer-Assisted Intervention*. Springer, 2015, pp. 234–241.
- [36] D. P. Kingma and M. Welling, "Auto-encoding variational bayes," in *International Conference on Learning Representations*, 2014.
- [37] A. B. L. Larsen, S. K. Sønderby, H. Larochelle, and O. Winther, "Autoencoding beyond pixels using a learned similarity metric," in *International Conference on Machine Learning*. PMLR, 2016, pp. 1558–1566.
- [38] B. Dai and D. Wipf, "Diagnosing and enhancing VAE models," in *International Conference on Learning Representations*, 2019.
- [39] S. R. Bowman, L. Vilnis, O. Vinyals, A. Dai, R. Jozefowicz, and S. Bengio, "Generating sentences from a continuous space," in *Proceedings of the 20th SIGNLL Conference on Computational Natural Language Learning*, S. Riezler and Y. Goldberg, Eds., Berlin, Germany, Aug. 2016, pp. 10–21.
- [40] Y. Song, J. Sohl-Dickstein, D. P. Kingma, A. Kumar, S. Ermon, and B. Poole, "Score-based generative modeling through stochastic differential equations," in *International Conference on Learning Representations*, 2021.
- [41] Q. Lyu and G. Wang, "Conversion between CT and MRI images using diffusion and score-matching models," *arXiv preprint arXiv:2209.12104*, 2022.
- [42] Y. Gong, "Gradient domain diffusion models for image synthesis," *arXiv preprint arXiv:2309.01875*, 2023.
- [43] C. R. Jack Jr., M. A. Bernstein, N. C. Fox, P. Thompson, G. Alexander, D. Harvey, B. Borowski, P. J. Britson, J. L. Whitwell, C. Ward, A. M. Dale, J. P. Felmlee, J. L. Gunter, D. L. Hill, R. Killiany, N. Schuff, S. Fox-Bosetti, C. Lin, C. Studholme, C. S. DeCarli, G. Krueger, H. A. Ward, G. J. Metzger, K. T. Scott, R. Mallozzi, D. Blezek, J. Levy, J. P. Debbins, A. S. Fleisher, M. Albert, R. Green, G. Bartzokis, G. Glover, J. Mugler, and M. W. Weiner, "The Alzheimer's disease neuroimaging initiative (ADNI): MRI methods," *Journal of Magnetic Resonance Imaging: An Official Journal of the International Society for Magnetic Resonance in Medicine*, vol. 27, no. 4, pp. 685–691, 2008.
- [44] A. Vaswani, N. Shazeer, N. Parmar, J. Uszkoreit, L. Jones, A. N. Gomez, L. Kaiser, and I. Polosukhin, "Attention is all you need," *Advances in Neural Information Processing Systems*, vol. 30, 2017.
- [45] M. J. Cardoso, W. Li, R. Brown, N. Ma, E. Kerfoot, Y. Wang, B. Murrey, A. Myronenko, C. Zhao, D. Yang *et al.*, "Monai: An open-source framework for deep learning in healthcare," *arXiv preprint arXiv:2211.02701*, 2022.
- [46] S. Xiao, M. Lewis, D. Mellor, M. McCabe, L. Byrne, T. Wang, J. Wang, M. Zhu, Y. Cheng, C. Yang, and D. S., "The China longitudinal ageing study: Overview of the demographic, psychosocial and cognitive data of the Shanghai sample," *Journal of Mental Health*, vol. 25, no. 2, pp. 131–136, 2016.
- [47] K. A. Ellis, A. I. Bush, D. Darby, D. De Fazio, J. Foster, P. Hudson, N. T. Lautenschlager, N. Lenzo, R. N. Martins, P. Maruff *et al.*, "The Australian Imaging, Biomarkers and Lifestyle (AIBL) study of aging: Methodology and baseline characteristics of 1112 individuals recruited for a longitudinal study of Alzheimer's disease," *International Psychogeriatrics*, vol. 21, no. 4, pp. 672–687, 2009.
- [48] F. Jessen, R. E. Amariglio, M. Van Boxtel, M. Breteler, M. Ceccaldi, G. Chételat, B. Dubois, C. Dufouil, K. A. Ellis, W. M. Van Der Flier *et al.*, "A conceptual framework for research on subjective cognitive decline in preclinical Alzheimer's disease," *Alzheimer's & Dementia*, vol. 10, no. 6, pp. 844–852, 2014.
- [49] K. Abdulrab and R. Heun, "Subjective Memory Impairment. A review of its definitions indicates the need for a comprehensive set of standardised and validated criteria," *European Psychiatry*, vol. 23, no. 5, pp. 321–330, 2008.
- [50] P. S. Aisen, R. C. Petersen, M. Donohue, and M. W. Weiner, "Alzheimer's disease neuroimaging initiative 2 clinical core: Progress and plans," *Alzheimer's & Dementia*, vol. 11, no. 7, pp. 734–739, 2015.
- [51] Y. Pan, M. Liu, C. Lian, T. Zhou, Y. Xia, and D. Shen, "Synthesizing missing PET from MRI with cycle-consistent generative adversarial networks for Alzheimer's disease diagnosis," in *Medical Image Computing and Computer Assisted Intervention*. Springer, 2018, pp. 455–463.
- [52] R. Rombach, A. Blattmann, D. Lorenz, P. Esser, and B. Ommer, "High-resolution image synthesis with latent diffusion models," in *Proceedings of the IEEE/CVF Conference on Computer Vision and Pattern Recognition*, 2022, pp. 10 684–10 695.
- [53] P. S. Aisen, R. C. Petersen, M. C. Donohue, A. Gamst, R. Raman, R. G. Thomas, S. Walter, J. Q. Trojanowski, L. M. Shaw, L. A. Beckett, C. R. Jack Jr, W. Jagust, A. W. Toga, A. J. Saykin, J. C. Morris, R. C. Green, M. W. Weiner, and Alzheimer's Disease Neuroimaging Initiative, "Clinical core of the Alzheimer's Disease Neuroimaging Initiative: Progress and plans," *Alzheimer's & Dementia*, vol. 6, no. 3, pp. 239–246, 2010.
- [54] J. C. Morris, "Clinical dementia rating: A reliable and valid diagnostic and staging measure for dementia of the Alzheimer type," *International Psychogeriatrics*, vol. 9, no. S1, pp. 173–176, 1997.
- [55] V. K. Shivamurthy, A. K. Tahari, C. Marcus, and R. M. Subramaniam, "Brain FDG PET and the diagnosis of dementia," *American Journal of Roentgenology*, vol. 204, no. 1, pp. W76–W85, 2015.
- [56] M. Dumba, S. Khan, N. Patel, L. Perry, P. Malhotra, R. Perry, K. Nijran, T. Barwick, K. Wallitt, and Z. Win, "Clinical 18F-FDG and amyloid brain positron emission tomography/CT in the investigation of cognitive impairment: Where are we now?" *The British Journal of Radiology*, vol. 92, no. 1101, p. 20181027, 2019.
- [57] C. M. Clark, J. A. Schneider, B. J. Bedell, T. G. Beach, W. B. Bilker, M. A. Mintun, M. J. Pontecorvo, F. Hefti, A. P. Carpenter, M. L. Flitter *et al.*, "Use of florbetapir-PET for imaging β -amyloid pathology," *JAMA*, vol. 305, no. 3, pp. 275–283, 2011.
- [58] J. Song, C. Meng, and S. Ermon, "Denoising diffusion implicit models," in *International Conference on Learning Representations*, 2021.

Functional Imaging Constrained Diffusion for Brain PET Synthesis from Structural MRI – *Supplementary Materials*

Minhui Yu, Mengqi Wu, Ling Yue, Andrea Bozoki, Mingxia Liu, *Senior Member, IEEE*



In what follows, we first visually show the synthetic PET images and difference maps generated by the proposed FICD and six competing methods from coronal and sagittal views. Then, we present the detailed information on the studied subjects used in this work, including (1) training and test sets in **Task 1** for image synthesis, (2) two validation sets in **Task 2** for disease progression prediction and **Task 3** for cognitive function prediction, and (3) training and test sets in **Task 4** for model generalization evaluation.

1 VISUALIZATION OF SYNTHETIC PET IN SAGITTAL AND CORONAL PLANES

We show the synthetic PET images and the corresponding difference maps in the sagittal view (Fig. S1) and the coronal view (Fig. S2), synthesized with MRI as input by our method and six competing methods. Note that each difference map is generated by calculating the difference between a synthetic PET and its ground truth. For comparison, their corresponding ground-truth PET and T1-weighted MRI inputs are also displayed.

2 MORE SUBJECT INFORMATION

To facilitate reproducible research, in Table S1, we list all the subject IDs from Alzheimer’s Disease Neuroimaging Initiative (ADNI) dataset [1] that we use for training and test the synthetic models in Task 1. In Table S2, we list all subjects from the Chinese Longitudinal Aging Study (CLAS) [2] and subjective memory concern (SMC) from the Alzheimer’s Disease Neuroimaging Initiative (ADNI) dataset [1] that are used in Tasks 2-3. Table S3 shows the list of the subjects from the Australian Imaging, Biomarkers and Lifestyle (AIBL) database [3] that are used for fine-tuning and test in Task 4.

REFERENCES

- [1] C. R. Jack Jr., M. A. Bernstein, N. C. Fox, P. Thompson, G. Alexander, D. Harvey, B. Borowski, P. J. Britson, J. L. Whitwell, C. Ward, A. M. Dale, J. P. Felmlee, J. L. Gunter, D. L. Hill, R. Killiany, N. Schuff, S. Fox-Bosetti, C. Lin, C. Studholme, C. S. DeCarli, G. Krueger, H. A. Ward, G. J. Metzger, K. T. Scott, R. Mallozzi, D. Blezek, J. Levy, J. P. Debbins, A. S. Fleisher, M. Albert, R. Green, G. Bartzokis, G. Glover, J. Mugler, and M. W. Weiner, “The Alzheimer’s disease neuroimaging initiative (ADNI): MRI methods,” *Journal of Magnetic Resonance Imaging: An Official Journal of the International Society for Magnetic Resonance in Medicine*, vol. 27, no. 4, pp. 685–691, 2008.
- [2] S. Xiao, M. Lewis, D. Mellor, M. McCabe, L. Byrne, T. Wang, J. Wang, M. Zhu, Y. Cheng, C. Yang, and D. S., “The China longitudinal ageing study: Overview of the demographic, psychosocial and cognitive data of the Shanghai sample,” *Journal of Mental Health*, vol. 25, no. 2, pp. 131–136, 2016.
- [3] K. A. Ellis, A. I. Bush, D. Darby, D. De Fazio, J. Foster, P. Hudson, N. T. Lautenschlager, N. Lenzo, R. N. Martins, P. Maruff *et al.*, “The Australian Imaging, Biomarkers and Lifestyle (AIBL) study of aging: Methodology and baseline characteristics of 1112 individuals recruited for a longitudinal study of Alzheimer’s disease,” *International Psychogeriatrics*, vol. 21, no. 4, pp. 672–687, 2009.

- M. Yu, M. Wu and M. Liu are with the Department of Radiology and BRIC, University of North Carolina at Chapel Hill, Chapel Hill, NC 27599 USA. M. Yu and M. Wu are also with the Joint Department of Biomedical Engineering, University of North Carolina at Chapel Hill and North Carolina State University, Chapel Hill, NC 27599, USA. L. Yue is with the Department of Geriatric Psychiatry, Shanghai Mental Health Center, Shanghai Jiao Tong University School of Medicine, Shanghai 200240, China. A. Bozoki is with the Department of Neurology, University of North Carolina at Chapel Hill, Chapel Hill, NC 27599, USA. Corresponding author: M. Liu (email: mxliu@med.unc.edu).

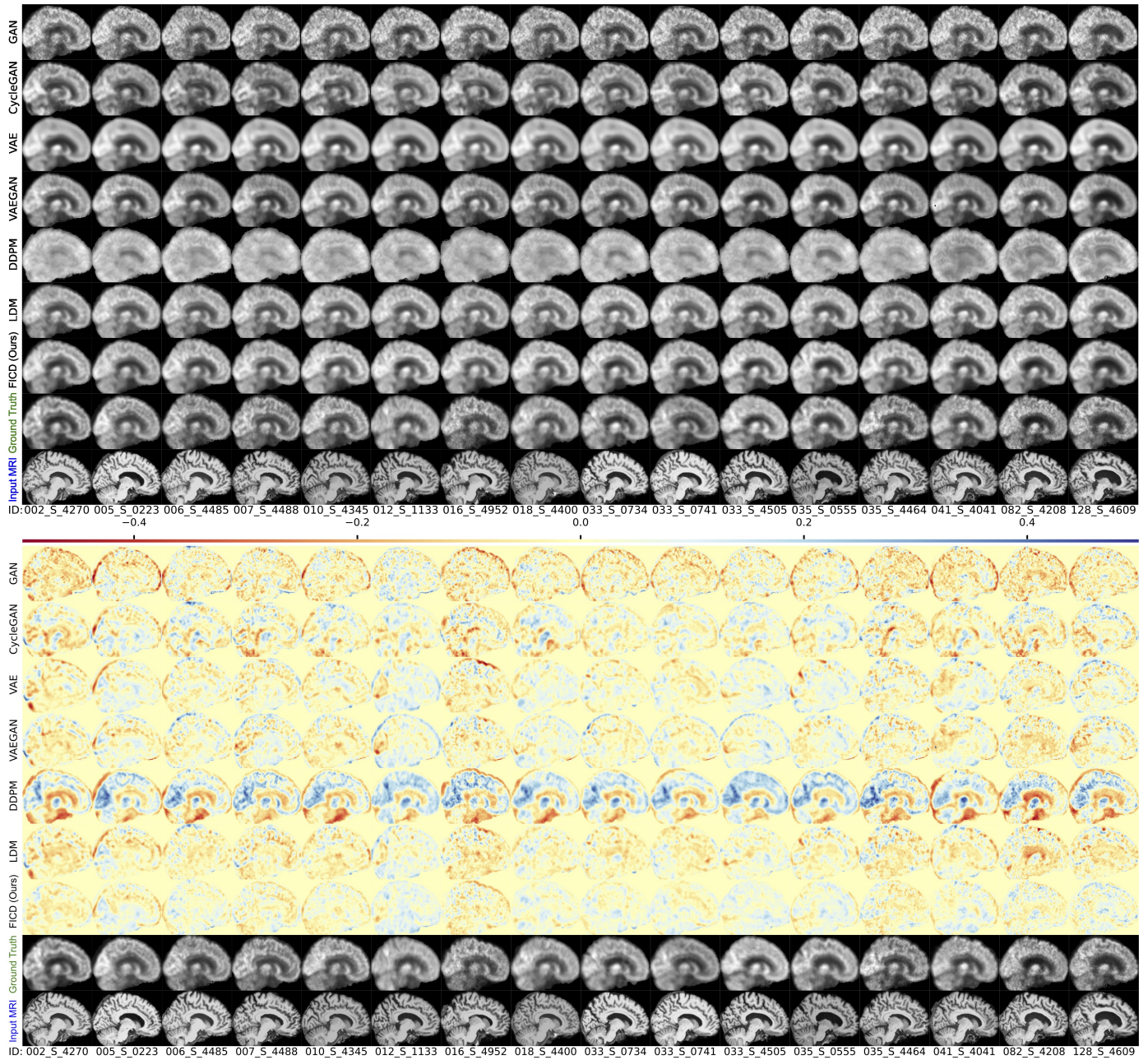


Fig. S1. Sagittal plane of synthetic PET images generated by the proposed FICD and six competing methods (top), using MRI scans from test data group of ADNI CN subjects as inputs. Each difference map illustrates the difference between a synthetic PET image and its ground truth (bottom).

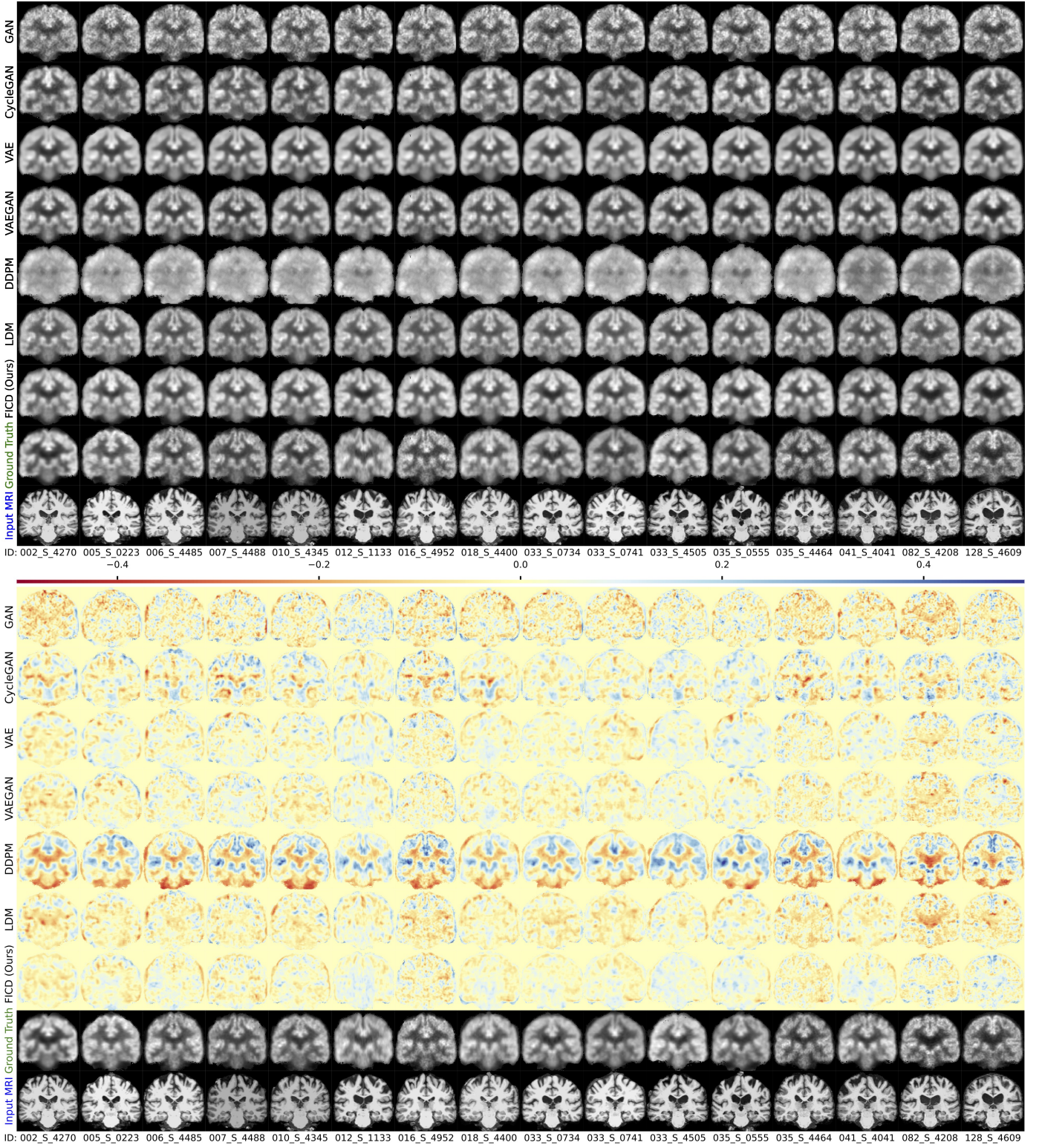


Fig. S2. Coronal plane of synthetic PET images generated by the proposed FICD and six competing methods (top), using MRI scans from test data group of ADNI CN subjects as inputs. Each difference map illustrates the difference between a synthetic PET image and its ground truth (bottom).

